The Astrophysical Journal, 763:71 (19pp), 2013 February 1 doi:10.1088/0004-637X/763/2/71

MULTIWAVELENGTH OBSERVATIONS OF GRB 110731A: GeV EMISSION FROM ONSET TO AFTERGLOW

M. Ackermann[1], M. Ajello[2], K. Asano[3], L. Baldini[4], G. Barbiellini[5,6], M. G. Baring[7], D. Bastieri[8,9], R. Bellazzini[4], R. D. Blandford[2], E. Bonamente[10,11], A. W. Borgland[2], E. Bottacini[2], J. Bregeon[4], M. Brigida[12,13], P. Bruel[14], R. Buehler[2], S. Buson[8,9], G. A. Caliandro[15], R. A. Cameron[2], P. A. Caraveo[16], C. Cecchi[10,11], E. Charles[2], R. C. G. Chaves[17], A. Chekhtman[18,74], J. Chiang[2], S. Ciprini[11,19], R. Claus[2], J. Cohen-Tanugi[20], J. Conrad[21,22,75], S. Cutini[23], F. D'Ammando[10,24,25], A. de Angelis[26], F. de Palma[12,13], C. D. Dermer[27], E. do Couto e Silva[2], P. S. Drell[2], A. Drlica-Wagner[2], C. Favuzzi[12,13], S. J. Fegan[14], W. B. Focke[2], A. Franckowiak[2], Y. Fukazawa[28], P. Fusco[12,13], F. Gargano[13], D. Gasparrini[23], N. Gehrels[29], N. Giglietto[12,13], F. Giordano[12,13], M. Giroletti[30], T. Glanzman[2], G. Godfrey[2], J. Granot[31], J. Greiner[32], I. A. Grenier[17], J. E. Grove[27], S. Guiriec[33], D. Hadasch[15], Y. Hanabata[28], M. Hayashida[2,34], E. Hays[29], R. E. Hughes[35], M. S. Jackson[22,36], T. Jogler[2], G. Jóhannesson[37], A. S. Johnson[2], J. Knödlseder[38,39], D. Kocevski[2], M. Kuss[4], J. Lande[2], S. Larsson[21,22,40], L. Latronico[41], F. Longo[5,6], F. Loparco[12,13], M. N. Lovellette[27], P. Lubrano[10,11], M. N. Mazziotta[13], J. E. McEnery[29,42], J. Mehault[20], P. Mészáros[43], P. F. Michelson[2], W. Mitthumsiri[2], T. Mizuno[44], C. Monte[12,13], M. E. Monzani[2], E. Moretti[22,36], A. Morselli[45], I. V. Moskalenko[2], S. Murgia[2], M. Naumann-Godo[17], J. P. Norris[46], E. Nuss[20], T. Nymark[22,36], M. Ohno[47], T. Ohsugi[44], N. Omodei[2], M. Orienti[30], E. Orlando[2], D. Paneque[2,48], J. S. Perkins[29,49,50,51], M. Pesce-Rollins[4], F. Piron[20], G. Pivato[9], J. L. Racusin[29], S. Rainò[12,13], R. Rando[8,9], M. Razzano[4,52], S. Razzaque[18,74], A. Reimer[2,53], O. Reimer[2,53], C. Romoli[9], M. Roth[54], F. Ryde[22,36], D. A. Sanchez[55], C. Sgrò[4], E. J. Siskind[56], E. Sonbas[29,57,58], P. Spinelli[12,13], M. Stamatikos[29,35], H. Takahashi[28], T. Tanaka[2], J. G. Thayer[2], J. B. Thayer[2], L. Tibaldo[8,9], M. Tinivella[4], G. Tosti[10,11], E. Troja[29,76], T. L. Usher[2], J. Vandenbroucke[2], V. Vasileiou[20], G. Vianello[2,59], V. Vitale[45,60], A. P. Waite[2], B. L. Winer[35], K. S. Wood[27], Z. Yang[21,22], D. Gruber[32], P. N. Bhat[33], E. Bissaldi[53], M. S. Briggs[33], J. M. Burgess[33], V. Connaughton[33], S. Foley[32,61], R. M. Kippen[62], C. Kouveliotou[63], S. McBreen[32,61], S. McGlynn[64], W. S. Paciesas[33], V. Pelassa[33], R. Preece[33], A. Rau[32], A. J. van der Horst[63,75], A. von Kienlin[32], D. A. Kann[32,64,65], R. Filgas[32,66], S. Klose[65], T. Krühler[67], A. Fukui[68], T. Sako[69], P. J. Tristram[70], S. R. Oates[71], T. N. Ukwatta[29,72], and O. Littlejohns[73]

[1] Deutsches Elektronen Synchrotron DESY, D-15738 Zeuthen, Germany
[2] W. W. Hansen Experimental Physics Laboratory, Kavli Institute for Particle Astrophysics and Cosmology, Department of Physics and SLAC National Accelerator Laboratory, Stanford University, Stanford, CA 94305, USA; kocevski@slac.stanford.edu, giacomov@slac.stanford.edu
[3] Interactive Research Center of Science, Tokyo Institute of Technology, Meguro City, Tokyo 152-8551, Japan
[4] Istituto Nazionale di Fisica Nucleare, Sezione di Pisa, I-56127 Pisa, Italy; johan.bregeon@pi.infn.it
[5] Istituto Nazionale di Fisica Nucleare, Sezione di Trieste, I-34127 Trieste, Italy
[6] Dipartimento di Fisica, Università di Trieste, I-34127 Trieste, Italy
[7] Department of Physics and Astronomy, Rice University, MS-108, P.O. Box 1892, Houston, TX 77251, USA
[8] Istituto Nazionale di Fisica Nucleare, Sezione di Padova, I-35131 Padova, Italy
[9] Dipartimento di Fisica e Astronomia "G. Galilei," Università di Padova, I-35131 Padova, Italy
[10] Istituto Nazionale di Fisica Nucleare, Sezione di Perugia, I-06123 Perugia, Italy
[11] Dipartimento di Fisica, Università degli Studi di Perugia, I-06123 Perugia, Italy
[12] Dipartimento di Fisica "M. Merlin" dell'Università e del Politecnico di Bari, I-70126 Bari, Italy
[13] Istituto Nazionale di Fisica Nucleare, Sezione di Bari, I-70126 Bari, Italy
[14] Laboratoire Leprince-Ringuet, École polytechnique, CNRS/IN2P3, Palaiseau, France
[15] Institut de Ciències de l'Espai (IEEE-CSIC), Campus UAB, E-08193 Barcelona, Spain
[16] INAF-Istituto di Astrofisica Spaziale e Fisica Cosmica, I-20133 Milano, Italy
[17] Laboratoire AIM, CEA-IRFU/CNRS/Université Paris Diderot, Service d'Astrophysique, CEA Saclay, F-91191 Gif sur Yvette, France
[18] Center for Earth Observing and Space Research, College of Science, George Mason University, Fairfax, VA 22030, USA; srazzaque@ssd5.nrl.navy.mil
[19] ASI Science Data Center, I-00044 Frascati (Roma), Italy
[20] Laboratoire Univers et Particules de Montpellier, Université Montpellier 2, CNRS/IN2P3, Montpellier, France
[21] Department of Physics, Stockholm University, AlbaNova, SE-106 91 Stockholm, Sweden
[22] The Oskar Klein Centre for Cosmoparticle Physics, AlbaNova, SE-106 91 Stockholm, Sweden
[23] Agenzia Spaziale Italiana (ASI) Science Data Center, I-00044 Frascati (Roma), Italy
[24] IASF Palermo, I-90146 Palermo, Italy
[25] INAF-Istituto di Astrofisica Spaziale e Fisica Cosmica, I-00133 Roma, Italy
[26] Dipartimento di Fisica, Università di Udine and Istituto Nazionale di Fisica Nucleare, Sezione di Trieste, Gruppo Collegato di Udine, I-33100 Udine, Italy
[27] Space Science Division, Naval Research Laboratory, Washington, DC 20375-5352, USA
[28] Department of Physical Sciences, Hiroshima University, Higashi-Hiroshima, Hiroshima 739-8526, Japan
[29] NASA Goddard Space Flight Center, Greenbelt, MD 20771, USA; eleonora.troja@nasa.gov
[30] INAF Istituto di Radioastronomia, I-40129 Bologna, Italy
[31] Centre for Astrophysics Research, Science and Technology Research Institute, University of Hertfordshire, Hatfield AL10 9AB, UK
[32] Max-Planck Institut für extraterrestrische Physik, D-85748 Garching, Germany; dgruber@mpe.mpg.de
[33] Center for Space Plasma and Aeronomic Research (CSPAR), University of Alabama in Huntsville, Huntsville, AL 35899, USA
[34] Department of Astronomy, Graduate School of Science, Kyoto University, Sakyo-ku, Kyoto 606-8502, Japan
[35] Department of Physics, Center for Cosmology and Astro-Particle Physics, The Ohio State University, Columbus, OH 43210, USA
[36] Department of Physics, Royal Institute of Technology (KTH), AlbaNova, SE-106 91 Stockholm, Sweden
[37] Science Institute, University of Iceland, IS-107 Reykjavik, Iceland
[38] CNRS, IRAP, F-31028 Toulouse cedex 4, France
[39] GAHEC, Université de Toulouse, UPS-OMP, IRAP, Toulouse, France
[40] Department of Astronomy, Stockholm University, SE-106 91 Stockholm, Sweden
[41] Istituto Nazionale di Fisica Nucleare, Sezione di Torino, I-10125 Torino, Italy
[42] Department of Physics and Department of Astronomy, University of Maryland, College Park, MD 20742, USA

[43] Department of Astronomy and Astrophysics, Pennsylvania State University, University Park, PA 16802, USA
[44] Hiroshima Astrophysical Science Center, Hiroshima University, Higashi-Hiroshima, Hiroshima 739-8526, Japan
[45] Istituto Nazionale di Fisica Nucleare, Sezione di Roma "Tor Vergata," I-00133 Roma, Italy
[46] Department of Physics, Boise State University, Boise, ID 83725, USA
[47] Institute of Space and Astronautical Science, JAXA, 3-1-1 Yoshinodai, Chuo-ku, Sagamihara, Kanagawa 252-5210, Japan
[48] Max-Planck-Institut für Physik, D-80805 München, Germany
[49] Department of Physics and Center for Space Sciences and Technology, University of Maryland Baltimore County, Baltimore, MD 21250, USA
[50] Center for Research and Exploration in Space Science and Technology (CRESST) and NASA Goddard Space Flight Center, Greenbelt, MD 20771, USA
[51] Harvard-Smithsonian Center for Astrophysics, Cambridge, MA 02138, USA
[52] Santa Cruz Institute for Particle Physics, Department of Physics and Department of Astronomy and Astrophysics, University of California at Santa Cruz, Santa Cruz, CA 95064, USA
[53] Institut für Astro- und Teilchenphysik and Institut für Theoretische Physik, Leopold-Franzens-Universität Innsbruck, A-6020 Innsbruck, Austria
[54] Department of Physics, University of Washington, Seattle, WA 98195-1560, USA
[55] Max-Planck-Institut für Kernphysik, D-69029 Heidelberg, Germany
[56] NYCB Real-Time Computing Inc., Lattingtown, NY 11560-1025, USA
[57] Department of Physics, Adıyaman University, 02040 Adıyaman, Turkey
[58] Universities Space Research Association (USRA), Columbia, MD 21044, USA
[59] Consorzio Interuniversitario per la Fisica Spaziale (CIFS), I-10133 Torino, Italy
[60] Dipartimento di Fisica, Università di Roma "Tor Vergata," I-00133 Roma, Italy
[61] School of Physics, University College Dublin, Belfield, Dublin 4, Ireland
[62] Los Alamos National Laboratory, Los Alamos, NM 87545, USA
[63] NASA Marshall Space Flight Center, Huntsville, AL 35812, USA
[64] Exzellenzcluster Universe, Technische Universität München, D-85748 Garching, Germany
[65] Thüringer Landessternwarte Tautenburg, D-07778 Tautenburg, Germany
[66] Institute of Experimental and Applied Physics, Czech Technical University in Prague, Horská 3a/22, 12800 Prague, Czech Republic
[67] Niels Bohr Institute, DK-2100 København Ø, Denmark
[68] National Astronomical Observatory of Japan, 2-21-1 Osawa, Mitaka, Tokyo 181-8588, Japan
[69] Solar-Terrestrial Environment Laboratory, Nagoya University, Nagoya 464-8601, Japan
[70] SCPS, Victoria University of Wellington, P.O. Box 60 Wellington NZ, New Zealand
[71] Mullard Space Science Laboratory, University College London, Holmbury St. Mary, Dorking, Surrey, RH5 6NT, UK
[72] Department of Physics and Astronomy, Michigan State University, Biomedical Physical Sciences Bldg. Room 3231, 567 Wilson Road, East Lansing, MI 48824, USA
[73] Department of Physics and Astronomy, University of Leicester, Leicester, LE1 7RH, UK
Received 2012 July 5; accepted 2012 December 1; published 2013 January 9

ABSTRACT

We report on the multiwavelength observations of the bright, long gamma-ray burst GRB 110731A, by the *Fermi* and *Swift* observatories, and by the MOA and GROND optical telescopes. The analysis of the prompt phase reveals that GRB 110731A shares many features with bright Large Area Telescope bursts observed by *Fermi* during the first three years on-orbit: a light curve with short time variability across the whole energy range during the prompt phase, delayed onset of the emission above 100 MeV, extra power-law component and temporally extended high-energy emission. In addition, this is the first GRB for which simultaneous GeV, X-ray, and optical data are available over multiple epochs beginning just after the trigger time and extending for more than 800 s, allowing temporal and spectral analysis in different epochs that favor emission from the forward shock in a wind-type medium. The observed temporally extended GeV emission is most likely part of the high-energy end of the afterglow emission. Both the single-zone pair transparency constraint for the prompt signal and the spectral and temporal analysis of the forward-shock afterglow emission independently lead to an estimate of the bulk Lorentz factor of the jet $\Gamma \sim 500$–550.

Key word: gamma-ray burst: individual (GRB110731A)

Online-only material: color figures

1. INTRODUCTION

Gamma-ray bursts (GRBs) are the most powerful explosions in the universe, initially releasing most of their energy in X-ray and gamma-ray on timescales lasting from a few seconds to a few minutes. Highly variable light curves across the energy bands in this prompt emission phase suggest an active central engine that drives the highly collimated GRB jet. The prompt emission is thought to be emitted by internal shocks, which are produced when shells of material collide within the jet. The variability within this emission, as observed in the prompt light curves, is thought to be due to intermittent central engine activity (Rees & Mészáros 1994).

However, the details of the emission mechanism that can explain the efficiency of the internal shocks are not understood. Fainter and longer-lived emission following the prompt phase, called the GRB afterglow (Mészáros & Rees 1997; Sari et al. 1998), has been observed at lower energies prior to *Fermi*, ranging from X-ray to optical and radio wavelengths. The first observations by the *Fermi* observatory of delayed and long-lived GeV emission relative to the prompt MeV emission (Abdo et al. 2009a, 2009b) have led to speculation (Kumar & Barniol Duran 2009, 2010; Ghisellini et al. 2010; De Pasquale et al. 2010; Corsi et al. 2010; Razzaque 2010) that the afterglow component may also include a significant amount of gamma-ray emission from the high-energy tail of the synchrotron radiation

[74] Resident at Naval Research Laboratory, Washington, DC 20375, USA.
[75] Royal Swedish Academy of Sciences Research Fellow, funded by a grant from the K. A. Wallenberg Foundation.
[76] NASA Postdoctoral Program Fellow, USA.

of the external forward shock. A contribution from the afterglow to the gamma-ray flux at such early times would indicate a significantly earlier onset of the interaction between the GRB blast wave and the circumburst medium (Blandford & McKee 1976), which is thought to be the source of the afterglow emission. The theoretical models of the underlying afterglow emission (Granot & Sari 2002) also constrain the physical parameters of the external shock such as the jet energy, bulk Lorentz factor, emission efficiency, and nature of the surrounding medium when optical-to-GeV data are fit simultaneously in this framework.

The *Fermi* observatory hosts two instruments, the Large Area Telescope (LAT), which covers an energy range from 20 MeV to up to more than 300 GeV (Atwood et al. 2009), and the Gamma-ray Burst Monitor (GBM), which is sensitive at lower energies from 8 keV to 40 MeV (Meegan et al. 2009). Together, LAT and GBM are capable of measuring the spectral parameters of GRBs across seven decades in energy. During the first three years on-orbit, the *Fermi*-LAT has detected more than 30 GRBs with high significance, but only four of these have benefited from simultaneous detections with the *Swift* Burst Alert Telescope (BAT), allowing for prompt follow-up with the narrow-field X-Ray Telescope (XRT) and Ultraviolet Optical Telescope (UVOT) on *Swift* (Gehrels et al. 2004). The first such burst was GRB 090510, a very bright short GRB for which the afterglow was observed contemporaneously by *Fermi*-LAT and by *Swift*/XRT and UVOT starting just 100 s after the burst trigger (De Pasquale et al. 2010). Multiwavelength data from GRB 090510 seem to favor an afterglow interpretation as their origin (De Pasquale et al. 2010; Corsi et al. 2010; Razzaque 2010). The second such burst was GRB 100728A, a very long burst for which *Fermi* revealed significant temporally extended emission out to 850 s post trigger, and *Swift* detected a series of strong X-ray flares in the XRT light curves. An internal shock scenario seems to reproduce well both the prompt emission and the later X-ray flares as well as temporally extended high-energy emission from GRB 100728A (Abdo et al. 2011). The third was GRB 110625A (Tam et al. 2012), which is a burst that triggered both BAT and GBM but which was outside of the LAT field of view during the prompt phase. However, thanks to the *Fermi* Autonomous Repoint Request (ARR) there was a joint XRT and LAT detection of the temporally extended emission.

In this paper we report on the analysis of the bright and long GRB 110731A, the fourth burst to benefit from joint *Fermi* and *Swift* observations, and one with the most comprehensive multiwavelength data of any LAT-detected GRB to date. Fortuitously, the burst was within the LAT field of view at the trigger time and caused an ARR. BAT also triggered on the burst and *Swift* was immediately repointed for XRT and UVOT observations. In addition, the burst was also observed by ground-based observatories, including the Microlensing Observations in Astrophysics (MOA) telescope at early and intermediate times, and the Gamma-ray Burst Optical/Near-Infrared Detector (GROND) at late times. Multiwavelength observations hence cover both the prompt phase and the temporally extended emission of GRB 110731A, from optical to GeV energies.

The paper is organized as follows: Section 2 includes a comprehensive description of the observations made by the various instruments that detected the burst's prompt and temporally extended emission, Section 3 gives the details of the data reduction and analysis for both the prompt emission and temporally extended emission for all telescopes, Section 4 reports the results of the prompt and temporally extended emission data analysis in the multiwavelength context, and Section 5 provides the discussion and interpretation of both the prompt and temporally extended emission results, and finally we draw our conclusions in Section 6.

Throughout the paper, times $t = T - T_0$ are given relative to the GBM time of trigger T_0, and the afterglow convention for the energy flux $F_{\nu,t} \propto \nu^{-\beta} t^{-\alpha}$ has been followed, where the energy index β is related to the differential photon index $\Gamma = \beta + 1$. The phenomenology of the burst is presented in the reference frame of the observer, unless otherwise stated. All the quoted errors are given at the 68% confidence level for one parameter of interest.

2. OBSERVATIONS

On 2011 July 31 at 11:09:29.94 (UT), GBM triggered on GRB 110731A which, due to the high peak flux of this burst, caused an ARR. GRB 110731A was already well within the LAT field of view, being only $\sim 3\overset{\circ}{.}3$ off axis so that the repointing had little impact on the prompt emission phase observations. The maneuver placed the spacecraft in pointing mode for 2.5 hr after the burst, allowing continuous LAT observation of the burst from the initial time of trigger until the first *Fermi* passage into the South Atlantic Anomaly (SAA) at 1400 s. The ARR continued for another 90 minutes after *Fermi* had exited the SAA at 3150 s, with the burst being well within the LAT field of view from 4000 s to 7400 s. No significant signal from GRB 110731A was found at these late times.

The best LAT localization of GRB 110731A is R.A. $= 18^{\rm h}41^{\rm m}00^{\rm s}$, decl. $= -28^\circ 31' 00''$ (J2000), with a 68% confidence error radius of $0\overset{\circ}{.}2$ (Abdo et al. 2009c).

GRB110731A triggered the *Swift*/BAT at 11:09:30.45 UT. *Swift* slewed immediately to the burst, and its narrow-field instruments, XRT and UVOT, began observations 56 s after the BAT trigger. An accurate afterglow position was rapidly determined by the UVOT as R.A. $= 18^{\rm h}42^{\rm m}00\overset{\rm s}{.}99$, decl. $= 28^\circ 32' 13\overset{''}{.}8$ (J2000; Oates et al. 2011), with an error radius of 0.5 arcsec (90% confidence).

XRT observations started while the spacecraft was settling at the end of the initial slew. The XRT began collecting data in Window Timing (WT) mode, as the source was bright ($\sim$100 cts s^{-1}), and automatically switched to Photon Counting (PC) mode when the count rate from the source decreased to $<$2 cts s^{-1}. Follow-up X-ray observations occurred during the following 24 days for a total net exposure of 600 s in WT mode and 75 ks in PC mode.

The UVOT took a short exposure with the *v* filter during the settling phase. This exposure was followed by a "finding chart" exposure with the *White* filter lasting 147 s. UVOT then began its usual procedure of cycling through its three visible filters (*v*, *b*, and *u*) and three *UV* filters (*uvw1*, *uvm2*, and *uvw2*) (Poole et al. 2008; Breeveld et al. 2010). The optical afterglow was detected in the *White*, *u*, *b*, and *v* filters, but not in the *UV* filters. The lack of detection in the *UV* filters is consistent with the measured redshift of $z = 2.83$ (Tanvir et al. 2011).

MOA observations began 3.3 minutes after the *Swift* trigger for GRB 110731A (GCN 12242; Tristram et al. 2011). Using a 61 cm Boller & Chivens telescope at the Mt. John University Observatory in New Zealand, *I*- and *V*-band images with 60 s exposures followed by 120 s exposures until 12:56 UT (105 minutes after the trigger) were obtained. The total numbers of *I* and *V* images are 39 and 35, respectively; however, due to the difficulty of photometry in the crowded field, we used only the 30 *I* and 19 *V* data points reported in Table 6.

After a weather-induced delay, the seven-color imager GROND (Greiner et al. 2008) mounted on the 2.2 m

MPG/ESO telescope at La Silla Observatory, Chile, observed GRB 110731A at a mean time of 2.74 days after the trigger. Two 30 minute observation blocks were obtained, which yielded an integration time of 4500 s in $g'r'i'z'$ and 3600 s in *JHK*. The mean seeing during the observations was 1.″3.

3. DATA ANALYSIS

3.1. Fermi

For the time-integrated and time-resolved spectral analysis of the prompt phase, both GBM and LAT data were used. The *Fermi*-LAT and GBM data may be retrieved from the *Fermi* Science Support Center archives.[77,78]

The GBM detectors were selected in the same fashion as outlined in Abdo et al. (2009c), Gruber et al. (2011), and Goldstein et al. (2012): we used the sodium iodide (NaI) detectors 0 and 3, and bismuth germanate (BGO) detector 0. We also used Time Tagged Events data (Meegan et al. 2009) for our spectral analysis with a temporal resolution of 64 ms, in the 8 keV to 40 MeV energy range, excluding the range around the NaI K-edge at 33.17 keV.

For the LAT, we first extracted "P7TRANSIENT"-class data from a circular region centered on the burst position with energy-dependent radius equal to a 95% containment of the point-spread function (PSF), see Abdo et al. (2009c) for details. To greatly reduce the numbers of gamma rays from the Earth limb we selected events with zenith angles less than 100°. We then followed the procedure described in Abdo et al. (2009c) to estimate the residual background and considered front- and back-converting events separately (Atwood et al. 2009). The results presented here were obtained using the *Fermi ScienceTools–v9r25p1* and *P7TRANSIENT_V6* instrument response functions (IRFs).

Besides the "P7TRANSIENT" data, we also extracted events using the so-called LAT low energy (LLE, $E \geqslant 10$ MeV) events selection criteria (Pelassa et al. 2010). The selection records those events that pass through the `GAMMA` filter, have a reconstructed track in the tracker pointing to a sky location that is roughly compatible with the GRB position (Atwood et al. 2009). By retaining very low energy events, this selection provides high statistics light curves that are useful for temporal analysis, see Section 4.1. We did not use LLE data for the spectral analysis since LLE and "P7TRANSIENT" data gave consistent results.

The LAT/GBM joint spectral fits were performed with the software package *XSPEC* version 12.7.0e (Arnaud 1996), and cross-checked with *rmfit* version 4.0rc1[79] (Kaneko et al. 2006; Abdo et al. 2009c). GBM Response Matrices v1.8 were used with both tools. For the fitting procedure, the PG-statistic (Arnaud et al. 2011) (S in the following) was used within *XSPEC*, while the Castor statistic (Ackermann et al. 2011) was used for *rmfit*.

For each time interval of interest, we compared the fit of several models that are listed below (differential fluxes are in photons/cm^2/keV/s).

1. A power law with an exponential cutoff (Comptonized model, hereafter COMP), whose differential photon flux is described by the equation

$$\mathrm{COMP}(E) = A \left(\frac{E}{E_{\mathrm{ref}}}\right)^{\Gamma_\alpha} \exp\left(-\frac{E}{E_0}\right), \qquad (1)$$

where A is the normalization amplitude, Γ_α is the photon index, E_{ref} is the reference energy fixed at 1 MeV, and E_0 is the cutoff energy.

2. A Band function, hereafter BAND, as defined in Band et al. (1993), where A is the normalization amplitude, Γ_α and Γ_β are the low- and high-energy power-law indices, and E_0 is the cutoff energy:

$$\mathrm{BAND}(E) = \begin{cases} A \left(\frac{E}{100\,\mathrm{keV}}\right)^{\Gamma_\alpha} \exp\left(-\frac{E}{E_0}\right) & E \leqslant (\Gamma_\alpha - \Gamma_\beta) E_0 \\ A \left[\frac{(\Gamma_\alpha - \Gamma_\beta) E_0}{100\,\mathrm{keV}}\right]^{\Gamma_\alpha - \Gamma_\beta} \left(\frac{E}{100\,\mathrm{keV}}\right)^{\Gamma_\beta} & \\ \times \exp(\Gamma_\beta - \Gamma_\alpha) & E > (\Gamma_\alpha - \Gamma_\beta) E_0. \end{cases} \qquad (2)$$

3. A COMP model plus a power law (COMP+PL):

$$\mathrm{COMP+PL}(E) = \mathrm{COMP}(E) + B \times \left(\frac{E}{100\,\mathrm{keV}}\right)^{\Gamma_\gamma}, \qquad (3)$$

where B is the normalization and Γ_γ the power-law photon index.

4. A BAND model plus a power law (BAND+PL):

$$\mathrm{BAND+PL}(E) = \mathrm{BAND}(E) + B \times \left(\frac{E}{100\,\mathrm{keV}}\right)^{\Gamma_\gamma}. \qquad (4)$$

5. A model with a sum of two independent Comptonized components (COMP+COMP) that in addition to the extra PL component provides also a second high-energy cutoff.

We remind the reader that the commonly referenced peak energy E_{peak} of the νF_ν spectrum can be computed as

$$E_{\mathrm{peak}} = (2 + \Gamma_\alpha) E_0 \qquad \text{in the COMP model.} \qquad (5)$$

The COMP (1) and BAND (2) models reported above were historically found to give very good empirical descriptions of GRB spectra (Band et al. 1993; Kaneko et al. 2006), with the COMP model having one less free parameter and providing a sharper decrease at high energies (usually in the ∼MeV range) than the BAND model. In order to check whether a different spectral component (meaning a different physical process and potentially a different location of the emission) could be responsible for the GeV emission observed in the LAT data, we added a power-law component to models (1) and (2), resulting the new models COMP+PL (3) and BAND+PL (4). Additionally, as some theoretical models predict that the high-energy GeV emission must be cut off owing to gamma–gamma pair production opacity considerations (see Section 5.1) we tested this hypothesis by considering the COMP+COMP model (5), that matches these characteristics while keeping a reasonable number of free parameters.

For each time interval we determined the best-fit model that provides a good description of the data with a minimal set of parameters, following the method described in Section 4.1 of Ackermann et al. (2011). In particular, we used the likelihood ratio test (LRT) to derive the significance of the improvement

[77] http://heasarc.gsfc.nasa.gov/FTP/fermi/data/gbm/triggers/
[78] http://fermi.gsfc.nasa.gov/ssc/data/access/
[79] *rmfit* for GBM and LAT analysis was developed by the GBM Team and is publicly available at fermi.gsfc.nasa.gov/ssc/data/analysis/.

of the fit when comparing a simpler model (the null hypothesis) with a more complex model (the alternative hypothesis). Using the PG-stat value, S, of the statistic and defining ΔS as the difference between the values of S obtained with the two models, the LRT gives the probability $P(\Delta S)$ that the observed ΔS has been obtained because of statistical fluctuations, on the assumption that the null hypothesis is the true model. Thus, if $P(\Delta S)$ is low the alternative hypothesis is to be preferred. We sampled the distribution of ΔS via 10 million Monte Carlo realizations of the burst spectrum with *XSPEC*. With such large statistics, we were able to compare pairs of models for probabilities down to $P(\Delta S) \sim 1 \times 10^{-7}$. Such simulations cannot account for systematic effects, for example due to the uncertainties in the responses of the instruments. Although a 10^{-4} probability would be formally very significant, we adopted a conservative threshold $P_{\rm th} = 1 \times 10^{-5}$, and we preferred the alternative models over the null hypothesis if $P(\Delta S) < P_{\rm th}$.

Since the count fluence of this burst is very high, we used the effective area correction factors (Abdo et al. 2009a) to account for possible calibration issues between the different detectors. We used the time-integrated spectrum (interval P1, see Section 4.1.2) and the BAND model to determine these factors, which were 0.85 for the BGO detectors and 0.96 for the NaI detectors, using the LAT spectrum as a reference. We applied these effective area corrections throughout the spectral analysis.

We explore the temporally extended emission from the burst in the LAT data running an unbinned likelihood analysis with the *Fermi ScienceTools–v9r25p1* and *P7TRANSIENT_V6* IRFs. Again, we estimated the residual particle background following the procedure described in Abdo et al. (2009c) for each sub-data selection. The model prepared for the likelihood analysis was then composed of a single power-law component for the burst itself, the particle background template and the template model "gal_2yearp7v6_v0.fits" for the Galactic diffuse emission[80] for which the normalization was held fixed during the fit.

In order to test the significance of the detection/light curve of the GRB at a particular time, without being dependent upon a subjective choice of time interval, we determined interval boundaries through the use of an algorithm that extends the time intervals until the likelihood test statistic is 18 in each bin. If a time interval exceeds the good time interval, an upper limit is reported and the computation steps to the next good time interval. The minimum number of events required in each interval is 8, to guarantee a reasonable number of degrees of freedom in the fit. Note that this method also optimizes the detection probability and provides the maximum number of time intervals on which the analysis can be run (more details may be found in Lott et al. 2012).

In order to fit the spectral energy densities (SEDs) using data from the different instruments (see Section 4.2.2 below), it was necessary to combine and adjust the LAT time intervals to have sufficient counts per bin and to match the observed features of the XRT light curve (see Section 4.2 below). We defined the new time intervals as follows: [8.3, 11.5] s (I, hereafter), [11.5, 55.0] s (II), [55.0, 227.0] s (III), and [227.0, 853.9] s (IV). We fit the LAT again over these time intervals using a slightly different background model in which the particle background and the Galactic diffuse emission are both estimated using the procedure described in Abdo et al. (2009c) so that we could extract separately the signal and background data to be used as input to *XSPEC* for the joint fits of the SEDs.

3.2. Swift

We retrieved the *Swift* data from the HEASARC archive[81] and processed them with the standard *Swift* analysis software (v3.8) included in the NASA's HEASARC software (HEASOFT, version 6.11) and the relevant calibration files.

We extracted BAT mask-weighted light curves and spectra in the nominal 15–150 keV energy range following the standard procedure (Sakamoto et al. 2008). The BAT data were not used for the spectral analysis of the prompt phase because the GBM data alone constrain Γ_α very well and because the cross-calibration between BAT and GBM is still not well understood and the subject is beyond the scope of this paper.

We extracted the XRT light curves and spectra in the nominal 0.3–10 keV energy range by applying standard screening criteria. All the XRT data products presented here are background subtracted and corrected for PSF losses, vignetting effects and exposure variations (see Evans et al. 2007, 2009).

UVOT photometric measurements were complicated by the crowded field. We obtained the source count rates from a circular source extraction region with a radius of 5″ (Poole et al. 2008; Breeveld et al. 2010). We estimated the background from nearby circular regions with radii of 20″, within which field sources were masked out. We also used *Swift* late-time observations to estimate the residual contribution of nearby objects, and to refine the afterglow photometry. For this reason, the last data point used in the light curve is at 1000 s. In order to better constrain the optical temporal decay we created a single light curve (see Figure 4) from all the UVOT filters by renormalizing each light curve to the v band (Oates et al. 2009), using flux conversion factors from Breeveld et al. (2011).

3.3. MOA

We performed the MOA data analysis using aperture photometry via the *SExtractor* package (Bertin & Arnouts 1996) to estimate the instrumental magnitudes of the objects in each image. We then compared these values to the late-time GROND data of the same field for zero-point determination of each of the MOA images. Since the MOA data were obtained with Bessell's *I*- and *V*-band filters, which have transmission curves similar to those of Johnson–Cousin's *I*- and *V*-band filters in combination with the CCD quantum efficiency curve, and GROND uses the *g'z'r'i'* filter system, we used the conversion table in Smith et al. (2002) to obtain a GROND equivalent *I*- and *V*-band magnitudes with which to perform this comparison. In order to reduce the systematic error in the zero-point determination, we selected only the top 30th percentile of brightest stars in the MOA images. Finally, we produced light curves for the same bright stellar objects in each of the MOA images for a final relative calibration. The resulting median Δm variations in these stellar light curves were used as additional corrections to the afterglow light curve that account for any errors in the zero-point determination of the individual images. We estimated the systematic error in the zero-point calibration of each image by measuring the standard deviation of the difference between the MOA and GROND equivalent *I*- and *V*-band magnitudes in each image. We then summed the statistical errors of the measured fluxes as returned by *SExtractor* in quadrature with this systematic error

[80] *Fermi* background models are available from the FSSC Web site at http://fermi.gsfc.nasa.gov/ssc/data/access/lat/BackgroundModels.html.

[81] http://heasarc.gsfc.nasa.gov/docs/swift/archive/

to obtain the error estimate in the final MOA flux density data. MOA results are given in Table 6, and as fluxes reported on the multiwavelength light curve shown in Figure 4.

3.4. GROND

We analyzed the GROND data analysis with a custom routine as described in Krühler et al. (2008) and Yoldaş et al. (2008), using *SExtractor* for background subtraction, and masking out bright sources. At the position of the afterglow, a faint source was visible in $r'i'z'$, but photometry was hindered by multiple nearby stars in the crowded field. Therefore, we obtained measurements for a second epoch on 2011 September 25, with identical exposure time, under improved conditions, to create a template image for image subtraction. We performed the image subtraction using *HOTPANTS*.[82] We used 60 different parameter settings in determining the Gaussian PSF kernel for the subtraction routine for each band, and chose the combination of parameters that resulted in the best subtraction of nearby stars near the afterglow position, as measured by the noise in the residual image at the afterglow position. In the residual image, the afterglow is strongly detected in r', still well detected in $i'z'$, only faintly detected in $g'JH$, and undetected in K. We calibrated the magnitudes of stars in the field against a Sloan Digital Sky Survey standard star field at similar R.A. observed just before the first epoch observations under photometric conditions. We performed the photometry using seeing-matched aperture photometry on the subtracted images with MIDAS.[83] We estimated the errors on the fluxes as the sum in quadrature of the calibration error, the statistical error of the detection, and the noise error of the image subtraction as determined by *HOTPANTS*. GROND results are given in Table 7, and as fluxes reported on the multiwavelength light-curve graph shown in Figure 4.

4. RESULTS

4.1. Prompt Phase

4.1.1. Light Curves and Timing Results

In Figure 1, we show the GBM and LAT light curves of the GRB prompt emission phase in several energy bands, from 8 keV to above 1 GeV. The light curves show a complex multi-peaked structure and have two interesting features: (1) the LAT emission at >10 MeV is slightly delayed (∼2.5 s) with respect to the GBM light curves, (2) a peak with high count rate is also present at 5.5 s in the LAT data that is also present in the NaI and BGO light curves.

Detailed analysis of the GBM data results in a $T_{90,\mathrm{GBM}}$ duration (Kouveliotou et al. 1993) in the 50 keV to 300 keV energy range of 7.3 ± 0.3 s, with a start time defined by $T_{05,\mathrm{GBM}} = 0.25 \pm 0.1$ s and an end time at $T_{95,\mathrm{GBM}} = 7.6 \pm 0.3$ s. A similar detection and duration analysis of the LLE light curve (>10 MeV) demonstrated that the LAT prompt phase detection starts later than observed in the GBM, at $T_{05,\mathrm{LLE}} = 2.5^{+0.3}_{-0.6}$ s, and lasts longer with $T_{90,\mathrm{LAT}} = 14.3^{-2.6}_{+17.0}$ s. These results for the LLE event selection are consistent with the findings for "P7TRANSIENT"-class events (>100 MeV) using an estimation of the total background following the procedure described in detail in Abdo et al. (2009c). Indeed, for the "P7TRANSIENT" events we found a comparable $T_{05,\mathrm{LAT}} = 3^{+0.3}_{-0.2}$ s. This analysis also revealed temporally extended emission up to $T_{95,\mathrm{LAT}} = 190^{+70}_{-170}$ s.

The LLE light curve was investigated using a Bayesian blocks algorithm (Scargle 1998; Scargle et al. 2012) to determine intervals over which the photon arrival rate has no statistically significant variations. By requiring a large statistical significance for the rate variations (to be less sensitive to background noise) four time intervals were found at [0, 2.44, 5.44, 6.06, 8.52] s and are highlighted in Figure 1. The upper boundary of the first time interval is at 2.44 s which is consistent with the previous estimate of the first signal significant detection in the LAT as reported above with other techniques. The four time intervals will be used in the next section for the time-resolved spectral analysis.

The flux peak at 5.5 s is observed across the whole energy spectrum so we examined it by calculating the cross-correlation functions (CCFs), as defined in Edelson & Krolik (1988), between energy bands to quantify the simultaneity of the emission. We calculated the CCF between the low-energy NaI and the LLE light curves, first considering the full prompt phase from −1 s to 8.52 s: the CCF has a local maximum at $0.3 \pm^{0.5}_{0.1}$ s, consistent with no lag. However, a second CCF maximum occurs at 5.2 s, possibly due to overlapping pulses and making the lag measurement subject to systematic uncertainties. The CCF thus suggests that the peak is indeed statistically coincident in time across the whole energy range, although it is less prominent at the very lowest energies in the NaI detectors than at high energies (the LAT events above 100 MeV).

We further characterized the variability of the emission by deriving a typical variability timescale for the burst emission following the light curve pulse deconvolution technique described in Bhat et al. (2012). We used the summed light curves from the four brightest NaI detectors, both the BGO detectors and the LLE data. The light curves were sub-divided into various energy bands, when possible, to estimate the energy dependence of the FWHM of the pulses. The median value of the FWHM of the pulses in the GBM NaI and BGO data over the $T_{90,\mathrm{GBM}}$ interval shows a weak dependence on energy, decreasing from 0.35 ± 0.02 s at ∼18 keV to 0.24 ± 0.01 s at 2 MeV with an average value 0.28 ± 0.02 s. The median value of the FWHM in the LLE data during the $T_{90,\mathrm{GBM}}$ interval is larger, 0.92 ± 0.15 s at ∼17 MeV. In a shorter time interval, [3.0 s, 7.6 s], that excludes the $T_{05,\mathrm{LAT}}$ time, the median value for the FWHM is 0.43 ± 0.03 s with a minimum of 0.147 ± 0.003 s, in the 8 keV–1 MeV range.

For each LAT "P7TRANSIENT"-class event, we estimated the probability of its being associated with the GRB using the *gtsrcprob Fermi* Science Tool. The probability computation takes into account the spectral and spatial distributions of all of the components in the source model, convolved with the response of the LAT as well as the exposure (all convolved with the effective PSF). The values of the model parameters are found via a maximum likelihood analysis (Mattox et al. 1996), and the probability of a particular event being attributed to a particular source component is proportional to the predicted counts density for the event by that component. The highest photon energy during the prompt phase is a 2.0 GeV event at 8.27 s, having a probability of 10^{-6} to be associated with the background. During the temporally extended emission phase, we note that a 3.4 GeV event at 435.96 s has a probability of $\sim 10^{-3}$ to be associated with the background.

[82] http://www.astro.washington.edu/users/becker/hotpants.html
[83] http://www.eso.org/sci/software/esomidas/

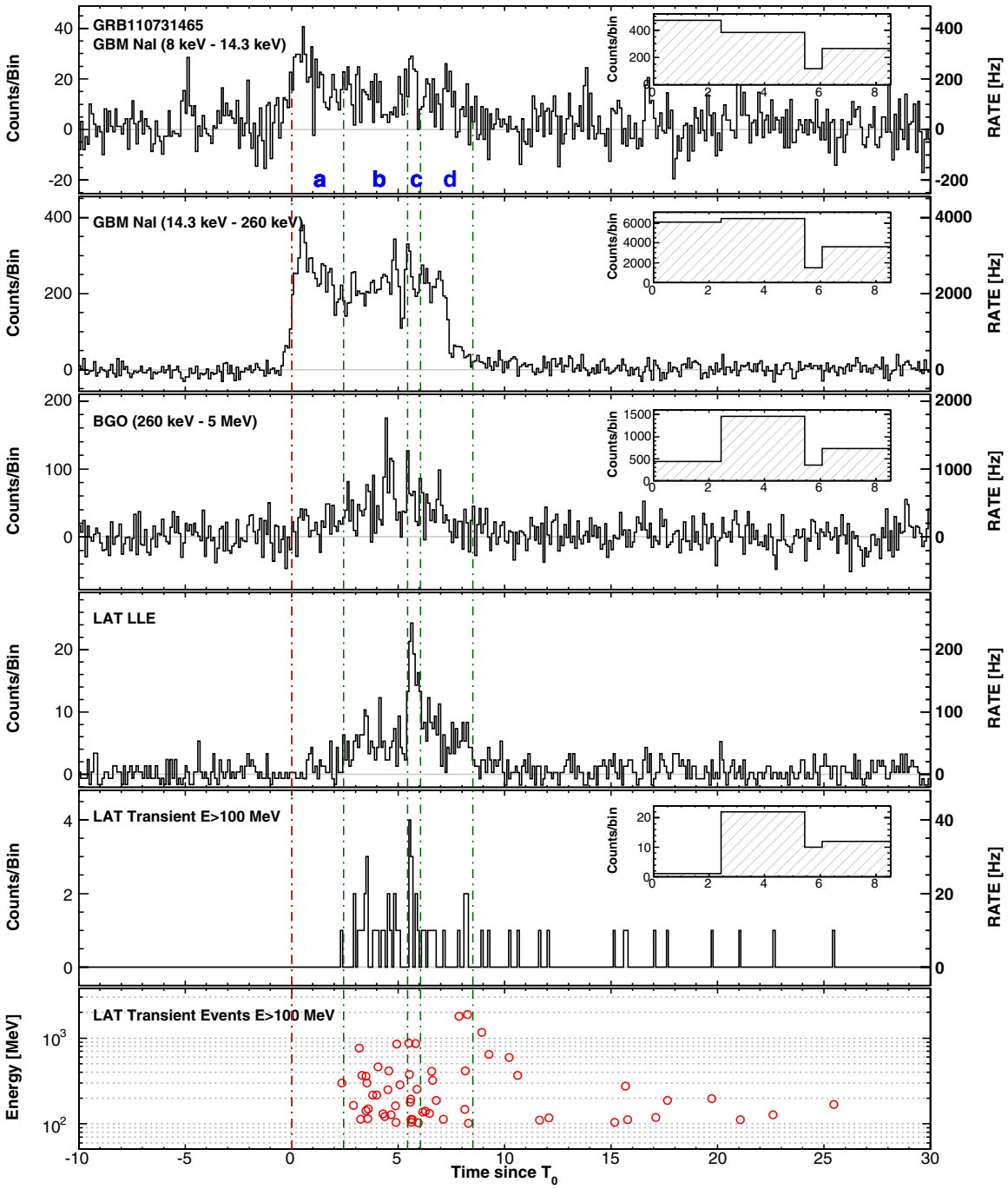

Figure 1. GBM and LAT light curves for the gamma-ray emission of GRB 110731A. The data from the GBM NaI detectors were divided into soft (8–14.3 keV) and hard (14.3–260 keV) bands to reveal similarities between the light curves at the lowest energies and for the LAT data. The first four light curves are background subtracted and have 0.1 s time binning. The fourth panel shows the LAT LLE light curve (Pelassa et al. 2010). The fifth panel shows the light curve for LAT "P7TRANSIENT"-class events for energies >100 MeV, with 0.5 s time binning. The sixth panel shows the energy and arrival time of LAT "P7TRANSIENT"-class events above 100 MeV. The vertical lines indicate the boundaries of the intervals *a, b, c, d*, used for the time-resolved spectral analysis for boundaries [0.00, 2.44, 5.44, 6.06, 8.52] s. The insets show the counts for each data set, binned using these intervals, to illustrate the numbers of counts considered in each spectral fit.

(A color version of this figure is available in the online journal.)

4.1.2. Spectral Analysis

We analyzed the burst emission spectrum over a number of time intervals.

1. The four intervals a, b, c, d which were determined by the Bayesian blocks analysis in Section 4.1.1.
2. Interval P1 ($a + b + c + d$ or [0, 8.52 s]) corresponds to the entire prompt emission phase.
3. Interval P2 ([3.0 s, 7.6 s]) spans the time range $T_{05,\mathrm{LAT}}$ to $T_{95,\mathrm{GBM}}$ in which we observe the maximum flux in both instruments.

We first considered the time interval P1 for the time-integrated spectral studies. We found that BAND is the preferred model. Both COMP+PL and BAND+PL provided only limited improvements in the fit. Comparing each one separately with BAND, we obtained a null hypothesis probability

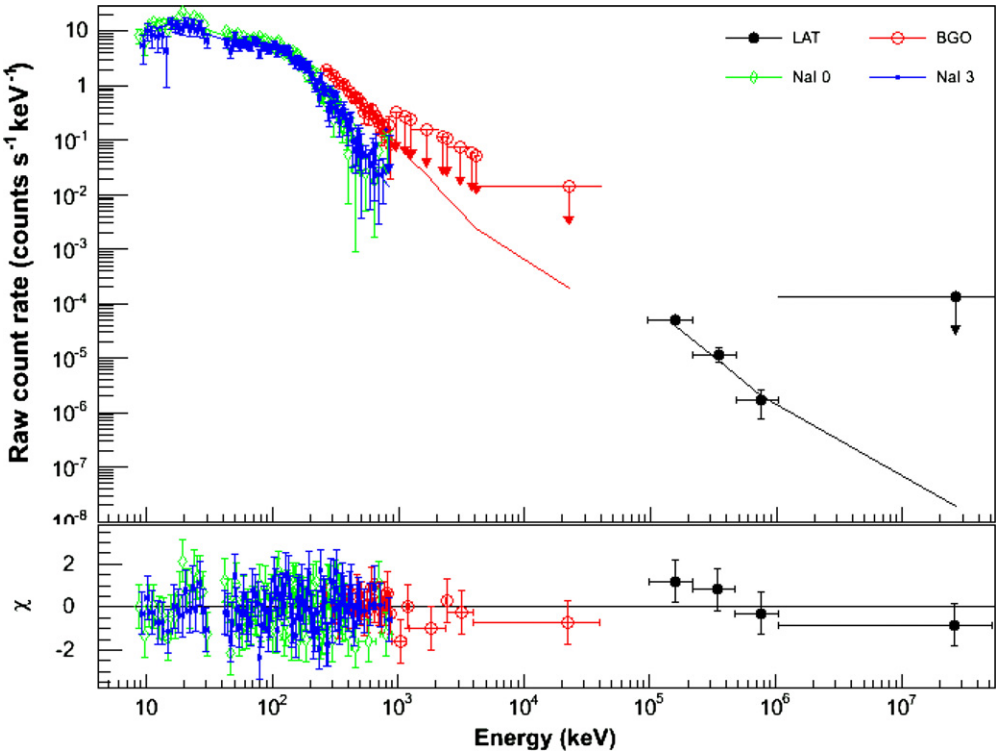

Figure 2. Joint spectral fitting of GBM and LAT data for the time interval P2, [3.0 s, 7.6 s]. The top panel shows the count spectra (points) and best-fit BAND+PL model (lines). The lower panel shows the residuals.

(A color version of this figure is available in the online journal.)

Table 1
Best-fit Parameters for All the Models for the Spectrum Obtained in the Interval P2, [3.0 s, 7.6 s]

Fitting Model	BAND	BAND+PL	COMP+PL	COMP+COMP
E_0 (keV)	349^{+31}_{-28}	155^{+20}_{-13}	198.8^{+21}_{-18}	191.1^{+21}_{-18}
Γ_α	$-0.74^{+0.04}_{-0.04}$	$0.03^{+0.15}_{-0.12}$	$-0.14^{+0.10}_{-0.10}$	$-0.10^{+0.12}_{-0.12}$
Γ_β	$-2.31^{+0.03}_{-0.03}$	$-2.40^{+0.10}_{-0.20}$	...	...
Extra Component				
Γ_γ	...	$-1.96^{+0.09}_{-0.05}$	$-1.89^{+0.02}_{-0.02}$	$-1.79^{+0.03}_{-0.03}$
Cutoff energy (MeV)	...	...	...	390^{+220}_{-120}
Fluence (10^{-5} erg cm^{-2})	$3.33^{+0.05}_{-0.05}$	$3.08^{+0.10}_{-0.10}$	$2.50^{+0.10}_{-0.10}$	$2.44^{+0.05}_{-0.08}$
PG-stat/dof	440.7/354	405.5/352	409.0/353	390.0/352

Note. The reference energy is fixed to 1 MeV. The fluence is evaluated for the 10 keV–10 GeV range.

$P(\Delta S) \simeq 1 \times 10^{-4}$ for both. The best-fit parameters for BAND were $\Gamma_\alpha = -0.89^{+0.03}_{-0.03}$, $\Gamma_\beta = -2.32^{+0.03}_{-0.03}$, $E_0 = 324^{+27}_{-25}$ keV with a corresponding fluence in the 10 keV–10 GeV energy band of $F = (4.56 \pm 0.05) \times 10^{-5}$ erg cm^{-2}, calculated in the rest frame.

To further investigate the significance of the additional power-law component, we performed a time-integrated spectral analysis on interval P2. Similarly to interval P1, the BAND model fitted the data reasonably well. This time, however, BAND+PL gave a large improvement and smaller residuals with respect to BAND, with $\Delta S = 35.2$ and a corresponding null hypothesis probability of $P(\Delta S) < 1 \times 10^{-7}$. Thus, the power-law component is required to account properly for the high-energy part of the spectrum. Moreover, the COMP+COMP model provided an even better fit for the same number of degrees of freedom, with $\Delta S = 15.5$ when compared to BAND+PL. Using the latter as null hypothesis we obtain $P(\Delta S) \simeq 3 \times 10^{-5}$. This latter result strongly suggests the presence of a cutoff in the high-energy part of the spectrum, although the null hypothesis probability is not formally below $P_{\rm th}$. A COMP+BAND or BAND+BAND model did not improve the fit over the COMP+COMP model. Furthermore the power-law slope of the high-energy BAND component could not be constrained due to limited statistics. The best-fit parameters of this time interval are given in Table 1, and the count spectrum corresponding to BAND+PL is shown in Figure 2.

We performed the time-resolved analysis in the four intervals a, b, c, d determined by the Bayesian blocks analysis (see Section 4.1.1): a Bayesian blocks algorithm ensures that the flux has no statistically significant variation over each interval, and hence provides a useful binning for studying the spectral evolution of the burst, in particular in the MeV-to-GeV range because the algorithm was run on the LLE light curve. We investigated in particular the presence of the power-law component

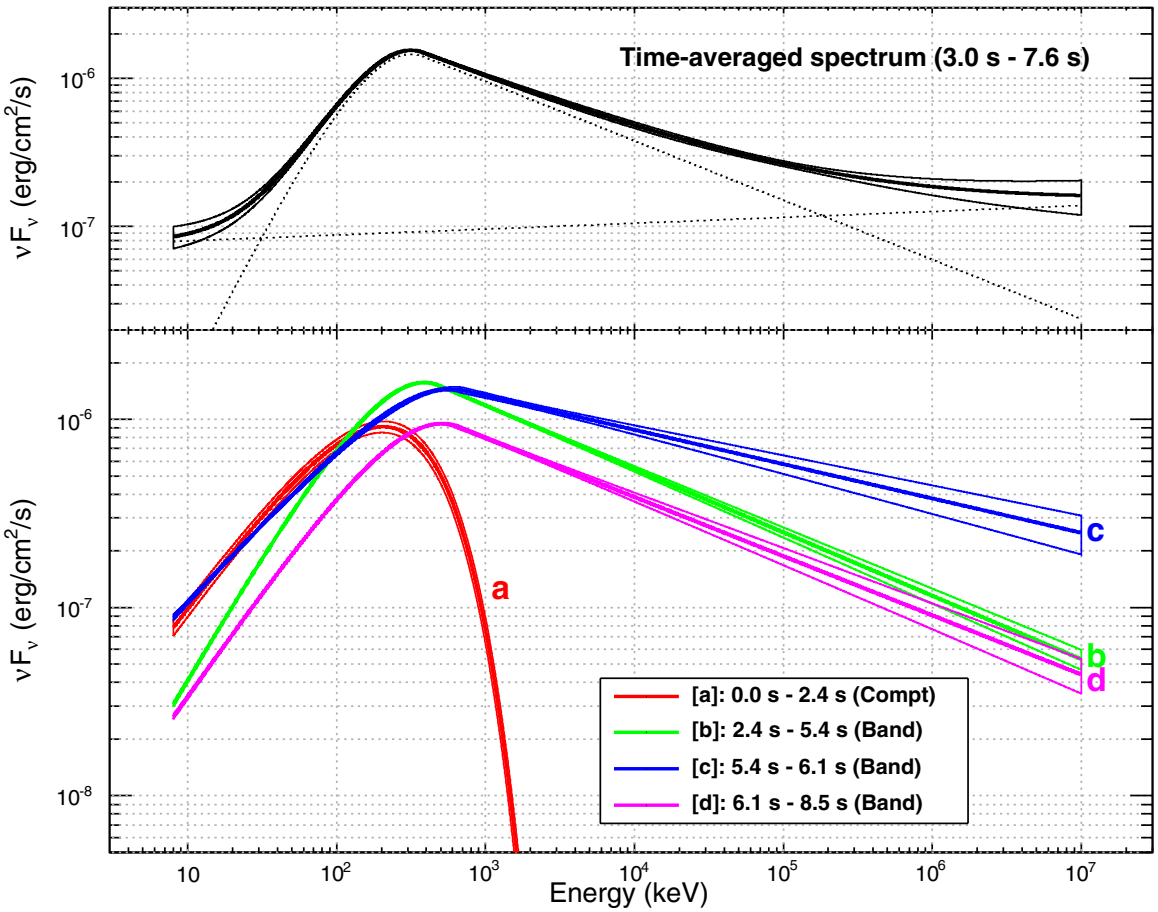

Figure 3. Top: the best-fit BAND+PL model for the time-integrated interval P2 plotted as a νF_ν spectrum. The two components are plotted separately as the dotted lines, and the sum of the components, representing the overall spectrum, is plotted as the heavy line. The $\pm 1\sigma$ ranges derived from the errors on the fit parameters are also shown. Bottom: the νF_ν model spectra (and $\pm 1\sigma$ error contours) plotted for each of the time bins considered in the time-resolved spectroscopy.
(A color version of this figure is available in the online journal.)

Table 2
Summary of GBM/LAT Joint Spectral Fitting by Best Model in Four Time Intervals

Time Interval from T_0 (s)	*a* (0–2.44)	*b* (2.44–5.44)	*c* (5.44–6.06)	*d* (6.06–8.52)
Best model	COMP	BAND	BAND	BAND
E_0 (keV)	188^{+22}_{-17}	285^{+30}_{-26}	683^{+270}_{-180}	446^{+91}_{-72}
Γ_α	$-0.92^{+0.05}_{-0.05}$	$-0.64^{+0.05}_{-0.05}$	$-1.15^{+0.05}_{-0.06}$	$-0.86^{+0.06}_{-0.06}$
Γ_β	...	$-2.34^{+0.04}_{-0.04}$	$-2.18^{+0.05}_{-0.06}$	$-2.31^{+0.04}_{-0.05}$
Fluence (10^{-5} erg cm^{-2})	$0.58^{+0.05}_{-0.06}$	$2.05^{+0.04}_{-0.04}$	$0.59^{+0.03}_{-0.03}$	$1.10^{+0.04}_{-0.04}$
PG-stat(dof)				
BAND (354)	...	417.4	365.3	389.1
COMP (353)	378.6	...	...	...
BAND+PL(352)	...	397.9	363.2	375.4
COMP+PL (353)	...	399.7	365.3	380.2
COMP+COMP (352)	...	389.8	360.2	377.7

Note. The fluences are evaluated for the range 10 keV–10 GeV for both instruments.

and of a high-energy cutoff. The best-fit spectral parameters for the preferred models are reported in Table 2, and the best models both for the time-resolved and time-integrated analyses are shown in Figure 3. The power-law component is not detected above the probability threshold in any of the intervals, likely due to the limited statistics. The results suggest, though, that a below-threshold power-law component may be present starting after the second interval. There is also marginal evidence of a high-energy cutoff in the second interval. Here we summarize the results from the time-resolved spectral studies.

1. *Interval a ([0, 2.44 s]).* The only model that was constrained by the data is COMP.
2. *Interval b ([2.44 s, 5.44 s]).* Adding a PL to BAND gave an improvement $\Delta S = 19.5$. Adopting BAND as null hypothesis, the corresponding probability is $P(\Delta S) \simeq 2 \times 10^{-5}$,

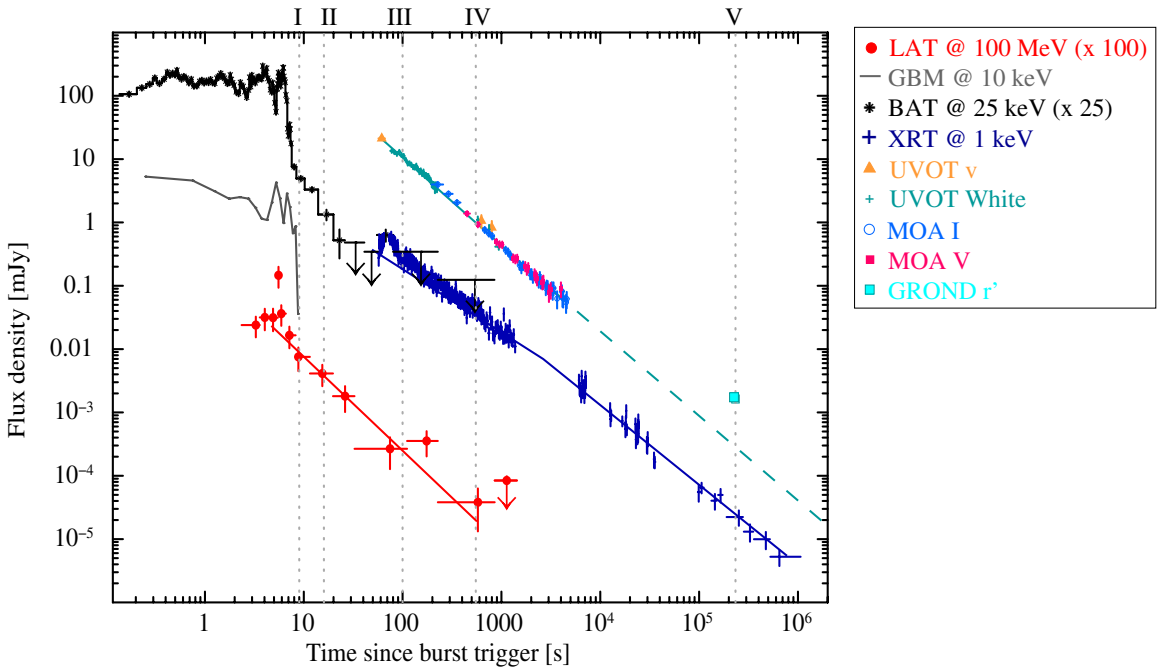

Figure 4. Multiwavelength light curves of GRB 110731A observations: vertical dotted lines define the time boundaries of the SEDs (indices I, II, III, IV, and V) studied in Section 4.2.2. The power-law index of the LAT light curve is $\alpha_{\rm LAT} = 1.55 \pm 0.20$. The XRT light curve follows a broken power law with $\alpha_{X,1} = 1.10 \pm 0.02$, $\alpha_{X,2} = 1.32 \pm 0.03$ and a break at $t_{\rm bk} = 4.6^{+2.6}_{-1.6}$ ks. The UVOT light curve is well fit by a single power law with decay slope $\alpha_{\rm opt} = 1.37 \pm 0.03$.
(A color version of this figure is available in the online journal.)

Table 3
LAT Time-resolved Spectroscopy Data, Photon Fluxes, and Photon Indices

Time Bins (s)	Energy Index	Photon Flux above 100 MeV (photons cm^{-2} s^{-1})	Test Statistic
(1) 2.35–3.59	-2.22 ± 0.39	$1.11 \pm 0.40 \times 10^{-3}$	73
(2) 3.59–4.56	-2.83 ± 0.60	$1.47 \pm 0.55 \times 10^{-3}$	53
(3) 4.56–5.47	-2.45 ± 0.49	$1.45 \pm 0.57 \times 10^{-3}$	68
(4) 5.47–5.67	-2.25 ± 0.41	$6.80 \pm 2.48 \times 10^{-3}$	88
(5) 5.67–6.58	-3.12 ± 0.68	$1.69 \pm 0.60 \times 10^{-3}$	90
(6) 6.58–8.27	-2.11 ± 0.37	$7.66 \pm 2.87 \times 10^{-4}$	70
(7) 8.27–11.54	-1.80 ± 0.31	$3.50 \pm 1.42 \times 10^{-4}$	73
(8) 11.54–19.73	-4.65 ± 1.24	$1.92 \pm 0.71 \times 10^{-4}$	41
(9) 19.73–32.60	-3.13 ± 0.82	$8.39 \pm 3.68 \times 10^{-5}$	27
(10) 32.60–110.97	-1.92 ± 0.38	$1.24 \pm 0.65 \times 10^{-5}$	20
(11) 110.97–227.04	-3.01 ± 0.68	$1.64 \pm 0.71 \times 10^{-5}$	17
(12) 227.04–853.89	-1.69 ± 0.35	$1.77 \pm 1.16 \times 10^{-6}$	16
(13) 853.89–1433.65	-2.25	$<3.9 \times 10^{-6}$	2

Note. The last entry is an upper limit assuming a power-law index of -2.25.

very close to the significance threshold. COMP+COMP marginally improved the fit with respect to BAND+PL, giving $\Delta S = 8.1$. Adopting the latter model as null hypothesis, we obtain $P(\Delta S) \simeq 3 \times 10^{-4}$.

3. *Interval c ([5.44 s, 6.06 s])*. BAND, BAND+PL, and COMP+COMP gave very similar values for S. Thus, from a statistical point of view, the more complex models are not favored over BAND. However, it is noteworthy that the best-fit parameters of the complex models gave results which are consistent with what we found for interval *b*.
4. *Interval d ([6.06 s, 8.52 s])*. BAND+PL fit the data slightly better than BAND alone, with $\Delta S = 13.7$. Adopting BAND as null hypothesis, we obtain $P(\Delta S) \simeq 3 \times 10^{-4}$. The high-energy cutoff of the COMP+COMP model is not well constrained.

4.2. Afterglow Modeling

4.2.1. Multiwavelength Afterglow Light Curves

The multiwavelength light curves for the seven instruments (LAT, GBM, XRT, BAT, UVOT, MOA, and GROND) that observed GRB 110731A are shown in Figure 4, and the corresponding data points are reported in Tables 3–7.

The LAT light curve in Figure 4 shows that the peak of the flux density is in the interval [5.47 s, 5.67 s], and that after 5.67 s, the flux decays smoothly during the whole temporally extended emission, following a power law with a fitted index $\alpha = 1.55 \pm 0.20$. The last time interval with a clear detection in the LAT data spans from 227.0 s to 853.9 s.

The BAT light curve shows many consequent adjacent peaks, from the trigger time to ~8.5 s. Faint, spectrally soft emission is

Table 4
Swift UVOT Data Table for the Individual Filters

Time (s)	Exposure (s)	Magnitude	Flux (mJy)	Filter
62	9	$13.08^{+0.06}_{-0.06}$	21.26 ± 0.71	v
627	20	$16.37^{+0.28}_{-0.22}$	1.03 ± 0.14	v
800	20	$16.86^{+0.43}_{-0.30}$	0.66 ± 0.13	v
1100	619	$17.48^{+0.34}_{-0.26}$	0.37 ± 0.06	v
12753	436	$20.30^{+3.36}_{-0.73}$	0.02 ± 0.06	v
1557278	1069878	>20.42	<0.03	v
552	20	$17.62^{+0.40}_{-0.29}$	0.36 ± 0.06	b
725	20	$18.02^{+0.59}_{-0.38}$	0.25 ± 0.05	b
1239	192	$18.91^{+0.68}_{-0.41}$	0.11 ± 0.03	b
15599	17857	$21.15^{+3.54}_{-0.73}$	0.01 ± 0.01	b
1557674	1070041	>21.00	<0.02	b
299	25	$17.28^{+0.33}_{-0.25}$	0.18 ± 0.02	u
324	25	$17.05^{+0.28}_{-0.22}$	0.22 ± 0.02	u
349	25	$16.98^{+0.26}_{-0.21}$	0.23 ± 0.02	u
374	25	$16.76^{+0.23}_{-0.19}$	0.28 ± 0.02	u
399	25	$17.11^{+0.29}_{-0.23}$	0.21 ± 0.02	u
424	25	$17.53^{+0.39}_{-0.29}$	0.14 ± 0.02	u
449	25	$17.57^{+0.41}_{-0.29}$	0.13 ± 0.02	u
474	25	$17.59^{+0.41}_{-0.29}$	0.13 ± 0.02	u
499	25	$17.35^{+0.34}_{-0.26}$	0.16 ± 0.02	u
524	25	$18.08^{+0.62}_{-0.39}$	0.08 ± 0.02	u
1001	620	>18.23	0.01 ± 0.01	u
21275	29621	>20.37	<0.01	u
439746	415954	>21.1	<0.01	u
976	620	>18.14	<0.05	$uvw1$
951	620	>19.12	<0.02	$uvm2$
989	793	>18.1	<0.04	$uvw2$

Notes. Time is the mid-time in exposure, in seconds, since BAT trigger. Exposure is the half-width of the integration duration in seconds. Magnitudes and flux densities have been corrected for Galactic extinction only. Upper limits are given at 3σ for both magnitudes and fluxes.

Table 5
Swift UVOT Data Table for the Co-added Exposures

Time (s)	Expo (s)	Magnitude	Flux (mJy)	Filter
80	10	$14.47^{+0.07}_{-0.06}$	3.13 ± 0.08	*white*
90	10	$14.55^{+0.07}_{-0.06}$	2.91 ± 0.08	*white*
100	10	$14.68^{+0.07}_{-0.07}$	2.59 ± 0.07	*white*
110	10	$14.87^{+0.07}_{-0.07}$	2.17 ± 0.06	*white*
120	10	$15.05^{+0.08}_{-0.07}$	1.83 ± 0.06	*white*
130	10	$15.08^{+0.08}_{-0.07}$	1.79 ± 0.05	*white*
140	10	$15.11^{+0.08}_{-0.07}$	1.74 ± 0.05	*white*
150	10	$15.29^{+0.08}_{-0.08}$	1.48 ± 0.05	*white*
160	10	$15.36^{+0.08}_{-0.08}$	1.38 ± 0.05	*white*
170	10	$15.52^{+0.09}_{-0.08}$	1.19 ± 0.04	*white*
180	10	$15.49^{+0.09}_{-0.08}$	1.22 ± 0.04	*white*
190	10	$15.6^{+0.09}_{-0.08}$	1.11 ± 0.04	*white*
200	10	$15.73^{+0.10}_{-0.09}$	0.98 ± 0.04	*white*
210	10	$15.83^{+0.10}_{-0.09}$	0.89 ± 0.03	*white*
220	10	$15.91^{+0.10}_{-0.09}$	0.83 ± 0.03	*white*
577	20	$17.12^{+0.16}_{-0.14}$	0.27 ± 0.02	*white*
750	20	$17.53^{+0.22}_{-0.18}$	0.19 ± 0.02	*white*
940	150	$18.26^{+0.14}_{-0.13}$	0.10 ± 0.01	*white*
1178	20	$19.32^{+1.93}_{-0.66}$	0.04 ± 0.01	*white*
1350	20	$18.48^{+0.55}_{-0.36}$	0.08 ± 0.01	*white*
6975	200	$20.27^{+0.73}_{-0.43}$	0.01 ± 0.01	*white*
104187	14049	>20.96	<0.01	*white*

Notes. Time is the mid-time in exposure, in seconds, since GBM trigger. Exposure is the half-width of the integration duration in seconds. Magnitudes and flux densities have been corrected for Galactic extinction only. Upper limits are given at 3σ for both magnitudes and fluxes.

detected out to ~30 s, and its temporal decay can be described by a power law with index $\alpha_{\rm BAT} = 2.3 \pm 0.3$. By shifting the reference time to the peak of the observed LAT emission at $t_{\rm pk} = 5.5$ s, i.e., shifting the reference to the onset of the forward shock, the decay slope changes to $\alpha_{{\rm BAT},t_{\rm pk}} = 1.25 \pm 0.15$. A rebrightening is visible between 50 s and 80 s, in coincidence with the first X-ray flare as seen on the multiwavelength light curve (Figure 4).

The X-ray light curve shows two X-ray flares, peaking at 70 s and 110 s, respectively. By excluding the interval of significant variability (from 56 s to 150 s) from the temporal fit, the light curve can be described by a simple power law with decay slope $\alpha_X = 1.189 \pm 0.007$ ($\chi^2 = 250$ for 228 dof). This model, though acceptable at a statistical level, systematically overestimates the late-time flux densities. A broken power law yields a significantly better result ($\chi^2 = 217$ for 226 dof) and shows no systematic trend in the residuals. The best-fit parameters are $\alpha_{X,1} = 1.10 \pm 0.02$, $\alpha_{X,2} = 1.32 \pm 0.03$, and $t_{\rm bk} = 4.6^{+2.6}_{-1.6}$ ks.

For the optical emission, the light curve we obtained using UVOT and MOA data altogether is very well fit by a single power law with decay slope $\alpha_{\rm opt} = 1.37 \pm 0.03$, as shown in Figure 4. For the UVOT data, we created a single filter light curve, the *White* light curve, by co-adding normalized version of the light curves for the seven UVOT filters. The multiwavelength light curve in Figure 4 shows just UVOT *White* and v data for clarity, as well as MOA data for the I and V bands. Data points for individual and co-added exposures are reported in Tables 4 and 5.

4.2.2. Broadband SED

We evaluated the SED at five epochs: 9 s (I), 16 s (II), 100 s (III), 550 s (IV), and 2.74 days (V). The SED times were selected in order to maximize the data coverage and minimize interpolation. For each epoch and instrument, a spectrum was extracted using the corresponding time interval, and scaled to the actual count rate at each time of interest. The time intervals were chosen in order to achieve a significant detection in the LAT energy band (epochs I–III), sufficient statistics in the X-ray spectrum (epoch IV) and to just match GROND observations for epoch V. Optical fluxes were interpolated, when necessary, by using the best-fit model for the light curve. At the GRB redshift of $z = 2.83$ the Lyman series absorption is redshifted to the observer frame wavelength range 3500–4700 Å. This mainly affects the UVOT b, u, and the GROND g' data points, which were therefore excluded from the spectral fits.

Each SED was fit with an absorbed power law or an absorbed broken power law, where the spectral slopes β_1 and β_2 were tied to $\beta_2 = \beta_1 - 0.5$, as predicted by the closure relations for a

Table 6
MOA Data Table Used in the *V* and *I* Bands

Time (s)	Magnitude[a]	Flux[b] (mJy)	Filter	Time (s)	Magnitude[a]	Flux[b] (mJy)	Filter
205	14.50 ± 0.10	$4.160^{+0.408}_{-0.372}$	*I*	2060	18.15 ± 0.19	$0.144^{+0.028}_{-0.023}$	*I*
268	14.87 ± 0.10	$2.960^{+0.293}_{-0.266}$	*I*	2143	19.15 ± 0.20	$0.082^{+0.017}_{-0.014}$	*V*
333	15.22 ± 0.10	$2.160^{+0.218}_{-0.198}$	*I*	2208	19.23 ± 0.20	$0.076^{+0.016}_{-0.013}$	*V*
428	16.76 ± 0.10	$0.746^{+0.071}_{-0.065}$	*V*	2271	19.33 ± 0.22	$0.070^{+0.015}_{-0.013}$	*V*
556	17.19 ± 0.10	$0.503^{+0.051}_{-0.046}$	*V*	2362	18.33 ± 0.20	$0.122^{+0.025}_{-0.021}$	*I*
656	16.29 ± 0.11	$0.800^{+0.089}_{-0.080}$	*I*	2426	18.14 ± 0.19	$0.146^{+0.028}_{-0.023}$	*I*
720	16.42 ± 0.12	$0.709^{+0.080}_{-0.072}$	*I*	2489	18.37 ± 0.20	$0.119^{+0.024}_{-0.020}$	*I*
785	16.54 ± 0.12	$0.639^{+0.074}_{-0.066}$	*I*	2573	19.47 ± 0.22	$0.061^{+0.014}_{-0.011}$	*V*
868	17.88 ± 0.12	$0.266^{+0.031}_{-0.028}$	*V*	2636	19.44 ± 0.23	$0.063^{+0.015}_{-0.012}$	*V*
933	17.97 ± 0.12	$0.244^{+0.029}_{-0.026}$	*V*	2787	18.59 ± 0.22	$0.096^{+0.022}_{-0.018}$	*I*
996	17.99 ± 0.12	$0.2410^{+0.029}_{-0.026}$	*V*	2851	18.51 ± 0.22	$0.104^{+0.023}_{-0.019}$	*I*
1082	17.09 ± 0.13	$0.384^{+0.050}_{-0.045}$	*I*	2914	18.53 ± 0.22	$0.102^{+0.023}_{-0.019}$	*I*
1145	17.16 ± 0.14	$0.359^{+0.049}_{-0.043}$	*I*	2999	19.87 ± 0.28	$0.042^{+0.013}_{-0.096}$	*V*
1210	17.30 ± 0.14	$0.315^{+0.044}_{-0.039}$	*I*	3127	19.77 ± 0.27	$0.047^{+0.013}_{-0.010}$	*V*
1293	18.52 ± 0.14	$0.148^{+0.021}_{-0.018}$	*V*	3214	18.59 ± 0.23	$0.097^{+0.023}_{-0.018}$	*I*
1358	18.55 ± 0.15	$0.143^{+0.021}_{-0.018}$	*V*	3277	18.74 ± 0.25	$0.084^{+0.022}_{-0.017}$	*I*
1421	18.53 ± 0.15	$0.146^{+0.021}_{-0.018}$	*V*	3342	18.59 ± 0.23	$0.096^{+0.023}_{-0.018}$	*I*
1506	17.68 ± 0.16	$0.222^{+0.035}_{-0.031}$	*I*	3637	19.00 ± 0.29	$0.066^{+0.020}_{-0.015}$	*I*
1569	17.81 ± 0.17	$0.198^{+0.033}_{-0.029}$	*I*	3978	19.73 ± 0.25	$0.048^{+0.013}_{-0.010}$	*V*
1634	17.70 ± 0.16	$0.219^{+0.035}_{-0.030}$	*I*	4061	18.71 ± 0.24	$0.086^{+0.0211}_{-0.017}$	*I*
1717	18.84 ± 0.17	$0.110^{+0.019}_{-0.016}$	*V*	4126	18.97 ± 0.28	$0.068^{+0.020}_{-0.015}$	*I*
1783	18.97 ± 0.18	$0.098^{+0.018}_{-0.015}$	*V*	4188	18.99 ± 0.28	$0.067^{+0.020}_{-0.015}$	*I*
1846	18.89 ± 0.17	$0.105^{+0.018}_{-0.016}$	*V*	4485	19.16 ± 0.30	$0.057^{+0.018}_{-0.014}$	*I*
1931	18.03 ± 0.18	$0.162^{+0.030}_{-0.025}$	*I*	4548	19.02 ± 0.28	$0.065^{+0.019}_{-0.015}$	*I*
1994	18.03 ± 0.19	$0.162^{+0.031}_{-0.026}$	*I*	...	...	...	...

Notes. Time is given since the GBM trigger. The exposure for each frame is 30 s.
[a] Extinction correction: $A_\lambda^V = 0.635$, $A_\lambda^I = 0.371$.
[b] Flux density.

Table 7
GROND Data Table; Seeing During the Observation Ranged from 1.″2 to 1.″5 Depending on the Band

Days	Filter	Mag (Vega)	Mag (AB)	Flux[a] (μJy)	Ext.[b] (Mag)	Exp. Time (s)
2.7404	g'	25.31 ± 0.24	25.25 ± 0.24	$0.54^{+0.13}_{-0.11}$	0.68	4500
2.7404	r'	23.66 ± 0.10	23.84 ± 0.10	$1.63^{+0.15}_{-0.14}$	0.47	4500
2.7404	i'	23.19 ± 0.11	23.60 ± 0.11	$1.82^{+0.20}_{-0.18}$	0.35	4500
2.7404	z'	22.59 ± 0.10	23.13 ± 0.10	$2.58^{+0.25}_{-0.23}$	0.26	4500
2.7404	*J*	21.66 ± 0.29	22.59 ± 0.29	$3.79^{+1.15}_{-0.88}$	0.15	3600
2.7404	*H*	20.92 ± 0.28	22.31 ± 0.28	$4.67^{+1.40}_{-1.08}$	0.10	3600
2.7404	*K*	>18.2	>20.1	<35.5	0.06	3600

Notes.
[a] Flux density, corrected for Galactic extinction.
[b] The Galactic extinction correction along the line of sight for $E(B-V) = 0.175$ (Schlegel et al. 1998) using a CCM Milky Way extinction law (Cardelli et al. 1989).

cooling break (Zhang & Mészáros 2004). The Galactic X-ray absorption and reddening were fixed to the values corresponding to $N_{\rm H} = 1.0\times\ 10^{21}$ cm^{-2} and $E(B-V) = 0.18$ (Oates et al. 2011), respectively. The intrinsic X-ray absorption was modeled by assuming an absorber with solar metallicity. To model the host intrinsic extinction we tested each of the Milky Way, Large Magellanic Cloud, or Small Magellanic Cloud (SMC) extinction law, as parameterized by Pei (1992). Limited statistics of our data did not permit any of these laws to be excluded or preferred.

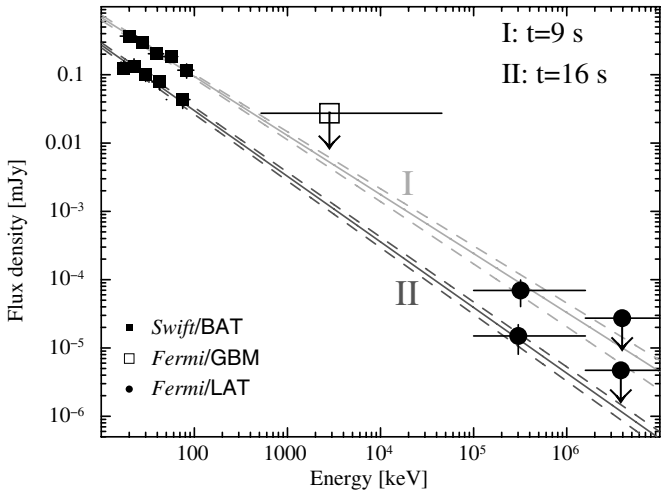

Figure 5. SEDs at epochs I and II. GBM BGO data upper limits at both epochs are very similar, so for clarity only the upper limit at epoch I is shown. The SEDs at epochs I and II are well fit by a power law with photon indices, $1.87^{+0.07}_{-0.11}$ and $1.95^{+0.07}_{-0.11}$, respectively. The continuous lines represent the best fit, and the dashed lines the 1σ ranges.

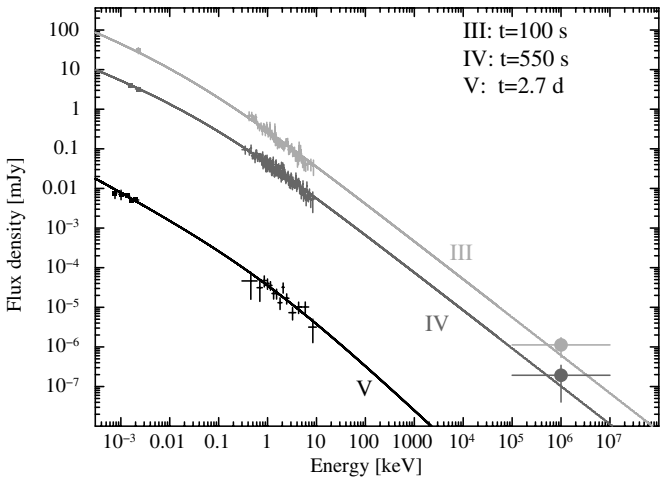

Figure 6. SEDs for epochs III, IV, and V. For epochs III and IV, the spectra are built using UVOT ($\sim 3 \times 10^{-3}$ keV), XRT ($\sim$0.5–10 keV), and LAT (10^5–10^7 keV) data. For epoch V, we have used the late-time GROND observations ($\sim 3 \times 10^{-3}$ keV) and XRT data. The solid lines show the fit of the wind model discussed in the text at each time, for the parameters reported in Table 8.

For epochs I and II, the SEDs are well fit by a single power-law spectrum over the whole energy range from the keV (BAT data) to the GeV (LAT data), as shown in Figure 5.

For epoch III the analysis was complicated by the presence of X-ray flares and also limited by the poor optical coverage at early times (cf. Figure 4). In order to estimate the afterglow underlying the observed flaring activity, we extracted the X-ray spectrum in interval [160 s, 227 s] and rescaled it by extrapolating the light curve best-fit model. We extracted the spectrum during the X-ray flares from 56 s to 150 s, and subtracted from the estimated afterglow contribution.

We also explored whether the observed SED evolution was consistent with the expected afterglow behavior in a wind-like density profile (Granot & Sari 2002). To this aim, we performed a joint fit by tying some parameters between the different epochs: we constrained the break energy to increase with time as $E_{\rm bk} \propto t^{0.5}$, and also held fix the host absorption and extinction as they are not expected to vary. We assumed a realistic model for the afterglow spectral shape, that is a smoothly broken power law of the form

$$F_\nu(E) \propto [(E/E_{\rm bk})^{-s\beta_1} + (E/E_{\rm bk})^{-s\beta_2}]^{-1/s}, \quad (6)$$

where the curvature parameter s was held fixed at 0.8. Epoch III was excluded from the fit procedure, but compared to the resulting best-fit model. SEDs and best fits using the wind model for epochs III, IV, and V are shown in Figure 6, and the best-fit results reported in Table 8 for all five epochs.

5. DISCUSSION AND INTERPRETATION

5.1. Prompt Emission

GRB 110731A was bright in the LAT data with its most prominent peak in interval c. The onset of the LAT emission is delayed by 2.5 s with respect to the GBM T_0, a time delay comparable to the few-seconds delay observed in most long-duration LAT GRBs. The time-resolved spectral analysis suggests that an additional, hard emission component becomes increasingly prominent with time. Indeed, in b, the BAND+PL model fits the spectrum better than a simple BAND, with a significance only slightly below our threshold. While an additional component cannot be statistically resolved in c, an additional power-law component improves the BAND-only fit in d as well, although with a rather low significance. By adopting the BAND+PL model for intervals b and d we can measure the ratio of the fluences of the power-law and BAND components, both measured in the 10 keV–10 GeV energy range. The ratio is 20% in interval b and 35% in interval d, respectively. This trend confirms an emerging picture, corroborated by spectral analysis of other bright LAT bursts with evidence of a power-law component in addition to the BAND component (namely GRB 090510, Abdo et al. 2010; GRB 090902B, Abdo et al. 2009a; and GRB 090926A, Ackermann et al. 2011), for which the flux of the additional power-law component grows with time, and most likely dominates in the temporally extended LAT emission beyond the prompt emission phase.

The origin of this additional spectral component is not yet fully understood. An early afterglow model (Kumar & Barniol Duran 2009, 2010; Ghisellini et al. 2010; De Pasquale et al. 2010; Corsi et al. 2010; Razzaque 2010), that is consistent with the above scenario, produces the power-law component from the forward shock of the GRB blast wave that propagates into the external medium surrounding the GRB (Mészáros & Rees 1997; Sari et al. 1998). The delayed onset of the LAT emission is explained as the time required for the forward-shock emission to become detectable in this scenario. In the context of the internal shock model (Rees & Mészáros 1994), the additional spectral component can arise due to Compton scattering of soft target photons by relativistic electrons (Mészáros & Rees 1994; Wang et al. 2009; Bošnjak et al. 2009; Toma et al. 2011). The 2.44 s delay for the LAT-detected emission in these scenarios would indicate GeV emission to be variable on a similar timescale and arising due to Compton emission from late internal shocks. Finally, hadronic emission, either proton/ion synchrotron radiation or photo-pion-induced cascade radiation, can produce an additional spectral component (Asano et al. 2009; Razzaque et al. 2010; Wang et al. 2009).

The delayed onset of the high-energy emission in the hadronic models is interpreted as due to the time required for proton/ion acceleration and cooling, as well as to the time required to form cascades. In particular, to generate

Table 8
Results of Broadband Fits of the SEDs

Model/Epoch	I (9 s)	II (16 s)	III (100 s)	IV (550 s)	V (2.7 day)
Power-law					
Index	$-1.87^{+0.11}_{-0.07}$	$-1.95^{+0.11}_{-0.07}$	...	...	...
Broken power law					
$\beta_{\rm opt}$	...	...	...	$-0.45^{+0.07}_{-0.09}$	$-0.66^{+0.03}_{-0.03}$
β_X	...	...	...	$-0.95^{+0.07}_{-0.09}$	$-1.16^{+0.03}_{-0.03}$
$E_{\rm break}$ (keV)	...	...	...	$0.04^{+0.03}_{-0.01}$	$\sim$0.8
s (curvature)	...	...	0.8	0.8	0.8
χ^2/dof	...	...	...	654/731	

Notes. For epochs I and II the simple power law is the best model. Epochs IV and V have been fitted together with a smoothly broken power law, with a curvature $s = 0.8$, $E_{\rm break} \sim t^{0.5}$, and $\beta_{\rm opt} = \beta_X + 0.5$. Epoch III was not part of the fitting procedure but we check that the data were compatible with the best-fit model obtained for epochs IV and V.

the 2.44 s delay in LAT the jet magnetic field needs to be $B' \approx 10^5 (\Gamma_0/500)^{-1/3} (t_{\rm onset}/2.44\,{\rm s})^{-2/3} (E_\gamma/100\,{\rm MeV})^{-1/3}$ G, with a jet bulk Lorentz factor Γ_0, in case of proton-synchrotron model and the corresponding isotropic-equivalent jet luminosity is $L_{\rm jet} \gtrsim 10^{57} (\Gamma_0/500)^{16/3} (t_{\rm onset}/2.44\,{\rm s})^{2/3} (E_\gamma/100\,{\rm MeV})^{-2/3}$ erg s^{-1} (Razzaque et al. 2010; Wang et al. 2009). While the hadronic models require a larger total energy than the leptonic models, the energy budget can be brought down to acceptable levels for a bulk Lorentz factor $\lesssim$500 (Abdo et al. 2010; Ackermann et al. 2011). In addition, the flat spectrum (index ~ -2) for the extra component is also favorable to the energy budget, and the observed low-energy (10 keV) excess (cf. Figure 3, top) could be additional evidence for a hadronic model. These two properties are very similar to the features already reported for the LAT burst GRB 090902B (Abdo et al. 2009a; Asano et al. 2010).

At a redshift $z = 2.83$, the peak isotropic-equivalent luminosity (10 keV–10 GeV) of GRB 110731A, as measured in interval c, is $L_{\rm iso,pk} = 6.3^{+0.3}_{-0.3} \times 10^{53}$ erg s^{-1}. The corresponding peak of the energy spectrum is at $E_{\rm pk} = (2 + \Gamma_\alpha) E_0 = 683^{+270}_{-180}$ keV, from the BAND fit. The total isotropic-equivalent energy (10 keV–10 GeV) over the full prompt phase (P1) is $E_{\rm iso} = 6.0^{+0.1}_{-0.2} \times 10^{53}$ erg, assuming a COMP+PL model. The BAND+PL fit to the same spectrum results in a somewhat larger $E_{\rm iso} = 7.6^{+0.2}_{-0.2} \times 10^{53}$ erg with a BAND $E_{\rm pk} = (2 + \Gamma_\alpha) E_0 \approx$ 300 keV. These values are broadly consistent with the empirical $L_{\rm iso,pk}$–$E_{\rm pk}$ (Yonetoku et al. 2004) and $E_{\rm iso}$–$E_{\rm pk}$ (Amati et al. 2009) relations for long GRBs. Another empirical relation between the luminosity and the spectral lags that we measured to be -41 ± 28 ms between two *Swift*/BAT energy bands is also satisfied (Norris et al. 2000; Ukwatta et al. 2012).

Constraining the bulk Lorentz factor, Γ_0, of the jet is a major challenge in GRB science. A constraint from the $\gamma\gamma$ pair production opacity argument can be used to derive a lower limit on Γ_0 if the spectrum does not have a cutoff and extends to the highest observed energy (Krolik & Pier 1991; Fenimore et al. 1993; Baring & Harding 1997; Lithwick & Sari 2001; Razzaque et al. 2004). For GRB 110731A, a 2.0 GeV photon was detected at 8.27 s. The spectrum in interval d that included this photon is preferably fit with a BAND+PL. We derive a lower limit, $\Gamma_{\rm min} \sim 600$, from $\tau_{\gamma\gamma} < 1$ using the above information and the median value of the FWHM of the pulses within the $T_{90,\rm GBM}$, $\Delta t = 0.35 \pm 0.02$ s, as the variability time in the single-zone emission approximation with a homogeneous distribution of photons (for a description of the method, see Abdo et al. 2010). The corresponding emission radius is $R \gtrsim \Gamma^2_{\rm min} c \Delta t (1+z)^{-1} \sim 10^{15}$ cm. In interval P2 we detect a high-energy cutoff with a significance only slightly below our threshold. This provides an opportunity to estimate Γ_0 as in GRB 090926A, by assuming that the cutoff is due to $\gamma\gamma$ pair production (Ackermann et al. 2011). We derive $\Gamma_0 = 530 \pm 10$, using the COMP+COMP model with a 390^{+220}_{-120} MeV folding energy for the high-energy component, and with $\Delta t = 0.43 \pm 0.03$ s, the median value of the FWHM of the pulses in P2. The maximum photon energy in this time interval is 0.9 GeV. Observe that while regions somewhat smaller than those inferred from these choices of Δt can be possible, since the pair opacity is a strong function of Γ_0, the values of the bulk Lorentz factor inferred here are only weakly dependent on the choice of Δt. Note that effects within the emission region such as radiation transport (Abdo et al. 2010) or a time-dependent increase of $\tau_{\gamma\gamma}$ and geometrical effects (Granot et al. 2008; Hascoët et al. 2012) can reduce the value of $\Gamma_{\rm min}$ or Γ_0 by a factor of up to three, even for a single-zone model. Indeed the $\Gamma_{\rm min}$ for the interval d reduces to a lower limit of $\sim$300 for the parameterization by Hascoët et al. (2012). Limits on the bulk Lorentz factor can be further relaxed for two-zone emission models, where GeV photons are emitted from a larger radius than the MeV photons (Zou et al. 2011; Hascoët et al. 2012). Such reductions in Γ_0 clearly can prove important for the viability of hadronic models, as discussed above.

5.2. LAT Temporally Extended Emission and Multiwavelength Afterglow

Thanks to the wealth of simultaneous multiwavelength data, we can test various afterglow models and extract the preferred model parameters. In particular, these observations can help constrain whether the temporally extended LAT emission originates in the forward shock that produces the late-time afterglow emission.

We discuss epoch IV first (cf. Figure 4) since the data are most constraining in this time interval. In Section 3.2 we observed that the optical flux ($\alpha_{\rm opt} = 1.37 \pm 0.03$) decays faster than the X-ray flux ($\alpha_{X,1} = 1.10 \pm 0.02$ or $\alpha_X = 1.189 \pm 0.007$), and in Section 4.2.2, we reported that the broadband SED is well fit by a smoothly broken power law at epoch IV. Both features favor a wind rather than interstellar medium (ISM) afterglow model, with a slow-cooling spectrum (Chevalier & Li 2000; Panaitescu & Kumar 2000). This results from an examination of the relations between the decay and spectral indices that describe flux evolution, $F_\nu \propto t^{-\alpha} \nu^{-\beta}$, at different energies of the afterglow synchrotron spectra (Granot & Sari 2002; Zhang et al. 2006). The break in the SED at epoch IV can be readily interpreted as a cooling break (ν_c) rather than a break due to the typical synchrotron frequency of the minimum energy electrons (ν_m), in both the slow- and fast-cooling spectra; the respective synchrotron indices below such breaks are $\beta = 2/3$ (slow-cooling) or $\beta = 3/2$ (fast-cooling). This is because the fast decay of the observed optical flux is contrary to (1) an increasing (ISM) or invariant (wind) flux behavior expected below ν_m in the slow-cooling spectrum; and (2) a much slower decay behavior, $F_\nu \propto t^{-1/4}$ (ISM or wind), expected below ν_m in the fast-cooling spectrum. Further investigation shows that the fast-cooling spectrum is disfavored at epoch IV, since (1) $\alpha_{X,1}$ or α_X and $\beta_{X,1}$ ($= 0.87 \pm 0.04$, derived as $\Gamma_X - 1$ before the temporal break) for the X-ray flux are both incompatible with the $F_\nu \propto t^{-1/4} \nu^{-1/2}$ behavior expected for $\nu_c < \nu_X < \nu_m$

(ISM or wind); and (2) $\alpha_{\rm opt}$ is incompatible with either $F_\nu \propto t^{1/6}$ (ISM) or $F_\nu \propto t^{-2/3}$ (wind) behavior for $\nu_{\rm opt} < \nu_c$. The spectral index $\beta_{X,\rm SED} = 0.95^{+0.09}_{-0.07}$ for $\nu_c < \nu_X$, fitting the broadband SED at epoch IV, is compatible, within 1σ–2σ, with $\beta_{X,1}$ and with the expected $\beta = (2/3)\alpha + 1/3$ behavior in the slow-cooling spectrum for $\alpha_{X,1}$ or α_X. While the above is common behavior for both the ISM and wind models, the observed $\alpha_{\rm opt}$ favors a $\beta = (2/3)\alpha - 1/3$ relation (wind) over a $\beta = (2/3)\alpha$ relation (ISM) when compared with the broadband SED fit result $\beta_{\rm opt,SED} = \beta_{X,\rm SED} - 0.5$. The expected optical spectral index is within 2σ of $\beta_{\rm opt,SED}$ in the wind model and deviates by more than 5σ from $\beta_{\rm opt,SED}$ in the ISM model. Thus our analysis favors a slow-cooling spectrum and wind environment for broadband data at epoch IV.

The broadband SED at 2.74 days, epoch V, has far less predictive power than the SED at epoch IV, with a single power law being statistically favored over a broken power law. Nevertheless, the joint fit to both SEDs using a smoothly broken power law, with tied indices but allowing the break frequency to increase as $\propto t^{1/2}$ between the SEDs as expected in the wind model, resulted in a good fit. This result further supports the wind model. A steeper decrease in the X-ray flux ($\alpha_{X,2} = 1.32 \pm 0.03$) after $4.6^{+2.6}_{-1.6}$ ks can be explained as the break frequency ν_c approaching the X-ray band with time and reaching ~1 keV at 2.74 days. An optical rebrightening is clearly visible in GROND data at epoch V without an accompanying rebrightening in X-ray, as observed in GRB 081029 (Nardini et al. 2011). The optical rebrightening could possibly originate from a two-component jet structure as modeled in GRB 030329 (Berger et al. 2003) and GRB 080319B (Racusin et al. 2008). However, the lack of data during the rise of the optical flux and sparse late-time data prohibit further study of the optical rebrightening in GRB 110731A.

The LAT temporally extended emission that is contemporaneous with the BAT and GBM detected emission at very early times, epochs I and II, can be fit with single power-law models to produce a broadband SED. The resulting photon indices, $1.87^{+0.07}_{-0.11}$ and $1.95^{+0.07}_{-0.11}$, respectively, are compatible with the measured X-ray photon index Γ_X at later times. In the context of the wind afterglow model, these two very early SEDs can be interpreted as being due to emission above ν_m in a fast-cooling spectrum ($\nu_c < \nu_m$) which subsequently turns into a slow-cooling spectrum ($\nu_m < \nu_c$) as ν_c increases with time and moves past ν_m, giving rise to the broken power-law SED at epoch IV. However, while the LAT flux decay index $\alpha_{\rm LAT} = 1.55 \pm 0.20$ is marginally consistent within 2σ with the later X-ray flux decay index $\alpha_{X,1}$ or α_X, the BAT flux decays ($\alpha_{\rm BAT} = 2.3 \pm 0.3$) at a much faster rate. A steeper decay of the BAT flux can be due to an emission component, such as high-latitude ($\theta > \Gamma_0^{-1}$) emission from the fireball (Kumar & Panaitescu 2000; Dermer 2004), in addition to the underlying afterglow emission. Indeed, fitting the BAT flux as $F_\nu \propto (t - t_{\rm pk})^{-\alpha}$, where $t_{\rm pk} = 5.5$ s was chosen to coincide with the brightest peak in the LAT light curve, results in a flux decay index ($\alpha_{{\rm BAT},t_{\rm pk}} = 1.25 \pm 0.15$) which is more compatible with $\alpha_{\rm LAT}$ and $\alpha_{X,1}$ or α_X, yet captures the steep decay of the BAT flux at very early time. Part of the LAT emission at ~5.5 s likely originates from such high-latitude emission and/or internal shocks. Indeed an extrapolation of the LAT afterglow flux at this time fails to reproduce all of the observed emission, as also noted for GRB 090510 (He et al. 2011).

Epoch III is rather complex with two weak X-ray flares. The most likely origin of the flares and a rebrightening of the emission detected by the BAT in coincidence with the first flare is late-time activity of the central engine (Zhang et al. 2006), as also implied by the noticeable variation of the spectrum from the underlying afterglow emission. The change in the afterglow synchrotron spectrum from the fast- to slow-cooling regime is expected to take place in this interval or earlier, since the SED in the next interval is best fitted by a broken power law as mentioned above.

Following the above discussion on the broadband SED of GRB 110731A for multiple epochs and flux decay behavior, two main features can be highlighted.

1. LAT temporally extended emission, as early as 8.3 s as seen in the first broadband SED, is compatible with the afterglow synchrotron emission in other bands.
2. A wind afterglow model is favored over an ISM model, from the behavior of the SEDs.

In the wind afterglow scenario, however, the onset of the afterglow needs to take place quite rapidly. There are several hints that this is the case: (1) the brightest peak in the LAT light curve dominating the νF_ν flux at all frequencies takes place as early as 5.5 s; (2) the absence of a brighter flux in the BAT or GBM at a later time; and (3) the LAT flux decays smoothly after 5.5 s. While the last point is quite obvious, the first two hints result from the fact that the bolometric flux of the forward-shock emission peaks at the deceleration time of the GRB fireball (Blandford & McKee 1976; Sari 1997; Ghisellini et al. 2010). In the case of an adiabatic fireball in the wind environment, the deceleration time is $t_{\rm dec} = (1+z)E_k/(16\pi m_p c^3 A\Gamma_0^4)$, where E_k is the isotropic-equivalent kinetic energy of the fireball during the decelerating phase and $A = 3.02 \times 10^{35} A_\star$ cm^{-1} is the wind parameter for a 10^{-5} $M_\odot$ yr^{-1} mass-loss rate in the wind of velocity 10^3 km s^{-1}, with $A_\star = 1$ as a scaling parameter (Chevalier & Li 2000). Note that formally the afterglow onset requires that $t_{\rm dec} \gtrsim T_{\rm GRB}$, where $T_{\rm GRB}$ is the duration of the prompt phase, for the "thin-shell" formula used here. Nevertheless, most of the emission detected by the GBM (50–300 keV) comes within the $T_{95,\rm GBM}$ (7.6 ± 0.3 s), which is similar to the deceleration timescale needed to explain the earliest broadband SEDs. Moreover, a fraction of the emission arriving later in the formal prompt phase may originate from the very early afterglow.

5.3. Afterglow Parameters in the Wind Model

Adopting the wind afterglow model and the broadband SED fit parameters of epoch IV, we derive the afterglow model parameters for GRB 110731A. The optical and X-ray flux decay indices constrain the electron acceleration index to be $p = (4/3)\alpha_{\rm opt} + 1/3 = 2.16 \pm 0.04$ and $p = (4/3)\alpha_{X,1} + 2/3 = 2.13 \pm 0.03$, respectively, from the $F_\nu \propto t^{-\alpha}\nu^{-\beta}$ relations. For the sake of simplification, we assume $p = 2.2$. We then use the parameterization by Granot & Sari (2002) for the break frequencies (ν_m, ν_c), the fluxes at the break frequencies (F_{ν_m}, F_{ν_c}), and the transition time (t_0) from the fast- to slow-cooling spectrum as

$$
\begin{aligned}
h\nu_m &= 3.5 \times 10^4 \epsilon_e^2 \epsilon_B^{1/2} E_{55}^{1/2} t_1^{-3/2}\ \text{keV},\\
h\nu_c &= 2.8 \times 10^{-8} \epsilon_B^{-3/2} A_\star^{-2} E_{55}^{1/2} t_1^{1/2}\ \text{keV},\\
F_{\nu_m} &= 7.1 \times 10^4 \epsilon_B^{1/2} A_\star E_{55}^{1/2} t_1^{-1/2}\ \text{mJy},\\
F_{\nu_c} &= 1.2 \times 10^{12} \epsilon_e^{1.2} \epsilon_B^{1.7} A_\star^{2.2} E_{55}^{1/2} t_1^{-1.7}\ \text{mJy},\\
t_0 &= 1.1 \times 10^7 \epsilon_e \epsilon_B A_\star\ \text{s}.
\end{aligned}
\tag{7}
$$

Here ϵ_e and ϵ_B are the usual micro-physical parameters (Sari et al. 1998; Granot & Sari 2002), $E_{55} = E_k/10^{55}$ erg, and $t_1 = t/10$ s.

Using the reference time $t_c \sim 550$ s for the cooling break in the SED, $h\nu_c \sim 0.04$ keV and $F_{\nu_c} \sim 0.5$ mJy, we obtain acceptable afterglow parameters for $t_{\rm dec} \sim 5.9$ s, the middle of the time interval with the brightest LAT peak, as

$$
\begin{aligned}
E_k &= 3.3\times10^{54}\left(\frac{A_\star}{0.05}\right)\left(\frac{t_{\rm dec}}{5.9\,{\rm s}}\right)\left(\frac{\Gamma_0}{500}\right)^4\ {\rm erg},\\
\epsilon_e &= 3.2\times10^{-3}\left(\frac{A_\star}{0.05}\right)^{-5/6}\left(\frac{t_{\rm dec}}{5.9\,{\rm s}}\right)^{-8/9}\left(\frac{\Gamma_0}{500}\right)^{-32/9}\\
&\quad\times\left(\frac{t_c}{550\,{\rm s}}\right)^{17/18}\left(\frac{h\nu_c}{0.04\,{\rm keV}}\right)^{17/18}\left(\frac{F_{\nu_c}}{0.5\,{\rm mJy}}\right)^{5/6},\\
\epsilon_B &= 1.1\times10^{-2}\left(\frac{A_\star}{0.05}\right)^{-1}\left(\frac{t_{\rm dec}}{5.9\,{\rm s}}\right)^{1/3}\left(\frac{\Gamma_0}{500}\right)^{4/3}\\
&\quad\times\left(\frac{t_c}{550\,{\rm s}}\right)^{1/3}\left(\frac{h\nu_c}{0.04\,{\rm keV}}\right)^{-2/3},\\
t_0 &= 19.5\left(\frac{A_\star}{0.05}\right)^{-5/6}\left(\frac{t_{\rm dec}}{5.9\,{\rm s}}\right)^{-5/9}\left(\frac{\Gamma_0}{500}\right)^{-20/9}\left(\frac{t_c}{550\,{\rm s}}\right)^{23/18}\\
&\quad\times\left(\frac{h\nu_c}{0.04\,{\rm keV}}\right)^{5/18}\left(\frac{F_{\nu_c}}{0.5\,{\rm mJy}}\right)^{5/6}\ {\rm s}. \qquad (8)
\end{aligned}
$$

Thus the fast- to slow-cooling transition takes place toward the end of epoch II, in which a single power law is a better fit to the broadband SED. The coasting bulk Lorentz factor $\Gamma_0 \sim 500$ is compatible with the value/lower limit obtained from the $\gamma\gamma$ opacity argument for the internal shocks. The kinetic energy is also a factor $\sim$5 larger than the isotropic-equivalent γ-ray energy $E_{\rm iso} = (6.8 \pm 0.1)\times10^{53}$ erg, which is compatible with the typically assumed ratio between the two energies. A deceleration time later than 5.9 s but earlier than $\sim$55 s can also be accommodated with acceptable parameter values in this scenario, without large deviations from the $\Gamma_0 \sim 500$ and $A_\star \sim 0.05$ values used in Equation (8). However, the fact that the broadband SED at epochs I and II can be fitted with power laws strongly argues in favor of an afterglow onset time before 8.3 s. The variations of the parameter values derived in Equation (8) are minimal in this case. With the parameters E_k and $A_\star$ fixed, a change of $t_{\rm dec}$ from 5.9 s to 8.3 s corresponds to $\Gamma_0 \sim 545$.

The maximum energy of the synchrotron photons, which is independent of the micro-physical parameters (see, e.g., Razzaque et al. 2010), can be written as

$$
\begin{aligned}
h\nu_{\rm max} &\approx 0.24\,\phi^{-1}(1+z)^{-1}\Gamma\,{\rm GeV}\\
&\sim 15\,\phi^{-1}t_2^{-1/4}\left(\frac{A_\star}{0.05}\right)^{-1/4}\left(\frac{E_k}{10^{54.5}\,{\rm erg}}\right)^{1/4}\ {\rm GeV}. \qquad (9)
\end{aligned}
$$

Here $\phi^{-1} \lesssim 1$ is the acceleration efficiency for electrons and $t_2 = t/100$ s. This equation applies to scenarios where lepton acceleration is gyroresonant and is radiation reaction limited by synchrotron cooling. In such cases, the maximum electron energy in the comoving jet frame is of the order of $m_e c^2$ divided by the fine structure constant, a result well known in the context of active galaxies (Guilbert et al. 1983) and the Crab Nebula (De Jager et al. 1996). Thus detection of a 3.4 GeV photon at $\sim$436 s from GRB 110731A (see the end of Section 4.1.1) is consistent with the maximum synchrotron photon energy for the afterglow parameters derived in Equation (8).

5.4. Comparisons with other GRBs

The sample of LAT-detected GRBs is still relatively small, with a detection rate of $\sim$8 yr^{-1} (Piron 2012). Here we briefly comment on the properties of GRB 110731A in comparison with other LAT-detected GRBs that were bright at GeV energies, and with GBM-detected GRBs in general. More detailed comparisons will be presented in a catalog of LAT GRBs that is in preparation. We also comment on the X-ray and optical afterglow of GRB 110731A in comparison with other GRBs.

The total (10 keV–10 GeV) isotropic-equivalent energy $E_{\gamma,\rm iso}$ of GRB 110731A falls in the middle of the distribution for LAT bursts with known redshifts; only GRB 100414A, GRB 091003, GRB 090328, and the short burst GRB 090510 have lower $E_{\gamma,\rm iso}$. In the 1 keV–10 MeV range, $E_{\gamma,\rm iso}$ for GRB 110731A is lower than for a number of GBM-only GRBs in the same redshift range. The fact that GRB 110731A was very close to the LAT boresight played a crucial role for its detection at $\gtrsim$100 MeV. An additional power-law component as in GRB 110731A has been detected in all bright LAT-detected GRBs and a cutoff in the power law for the $\gtrsim$100 MeV energy range has been reported in GRB 090926A (Ackermann et al. 2011) in addition to the present case. The value of the jet bulk Lorentz factor and its lower limits has been calculated, using $\gamma\gamma$-opacity argument for simple single-zone model, in the range of $\gtrsim$200 to $\gtrsim$1000 for bright LAT GRBs (Abdo et al. 2009a, 2009b, 2010; Greiner et al. 2009; Ackermann et al. 2011; Cenko et al. 2011). The $\Gamma_0 \sim 500$ value that we derived for GRB 110731A using the same argument is in the middle of this range. Note that uncertainties in underlying emission modeling may scale down these values by a factor two to three (Section 5.1). Although the current sample is rather small, a cutoff in the BAND or PL spectrum could be one reason for the LAT non-detection of a number of bright GBM bursts within the LAT field of view (Ackermann et al. 2012).

Temporally extended high-energy emission detected in GRB 110731A is quite common among LAT-detected GRBs, showing a smooth power-law decay of the flux. The flux decay index, however, is not the same among bursts but varies between $\sim$1 and $\sim$1.5 (Ghisellini et al. 2010). The common behavior of the temporally extended LAT flux is compatible with afterglow emission, but a direct model comparison with contemporaneous multiwavelength data sets is possible only for the short burst GRB 090510 (De Pasquale et al. 2010; Abdo et al. 2010) and for the current long burst GRB 110731A.

The X-ray afterglow of GRB 110731A does not display the "canonical" steep-, flat-, and normal-decay behavior (Nousek et al. 2006) observed in $\sim$40% of all long GRBs detected by *Swift*. This trend for GRB 110731A is also observed in other LAT bursts with early-time *Swift*/XRT observations such as GRB 100728A (Abdo et al. 2011) and GRB 110625A (Tam et al. 2012), and may suggest that the afterglows of LAT bursts tend to be dominated by the bright forward-shock emission rather than prolonged episodes of energy injection.

We have studied the optical afterglow of GRB 110731A using the method of Kann et al. (2006) and compared it with other well-measured afterglows (Kann et al. 2006, 2010, 2011). As

the data quality in the optical is not sufficient to allow a fit with all parameters free, we fix the underlying spectral slope to the value derived from the broadband X-ray-to-optical fit, $\beta = 0.66$. A free fit to the optical data alone results in a similar value, $\beta \approx 0.7$, but with very large errors. Assuming an SMC-like dust density, we derive an extinction $A_V = 0.24 \pm 0.06$ (note that this error is somewhat underestimated due to the constrained spectral slope). Alternatively, without dust, the optical data yield a red spectral slope of $\beta = 1.41 \pm 0.18$. Using this extinction value and the redshift, we find a magnitude correction (Kann et al. 2006) of $dRc = -3.46^{+0.17}_{-0.23}$ (alternatively, $dRc = -3.09 \pm 0.13$ without extinction). Using the known SED, we are able to create a compound R-band light curve, to which we add GCN data (Malesani et al. 2011; Tanvir et al. 2011). The resulting light curve spans from 32 s to ≈1.5 days after the GRB, and reaches a peak at the 9th magnitude, implying that this is initially an exceptionally bright afterglow. Comparing the known sample of optical afterglows with prompt-emission detections in the high-MeV/GeV range (including one *AGILE* GRID GRB, GRB 080514B; Giuliani et al. 2008; Rossi et al. 2008; McBreen et al. 2010; Cenko et al. 2011) we find that while some afterglows are among the most luminous known (GRB 090923, GRB 090926A), the others are of average luminosity at $t = 1$ day, including GRB 110731A. The span is 4 magnitudes, and if one extrapolates the steep late decay of the short GRB 090510 (Nicuesa Guelbenzu et al. 2012), the span reaches about 10 magnitudes. The very early detection of the afterglow of GRB 110731A also allows us for the first time to compare the brightness at 0.001 days (normalized at $z = 1$) for a LAT-detected GRB, we find $R = 10.5$. Coupled with the unbroken decay from the earliest detection on, this makes it one of the brightest forward-shock-dominated afterglows known (Kann et al. 2010).

Our broadband spectral and temporal modeling, including LAT data, favors a circum-burst medium with a wind-like density profile and an afterglow onset time $\lesssim$9 s after trigger. This is the first time that a LAT-detected long GRB could have such an early onset time estimated using multiwavelength data. The corresponding bulk Lorentz factor value $\Gamma_0 \sim 500$, deduced from the deceleration timescale of the fireball, is also better motivated for GRB 110731A. With a constant density ISM environment and by assuming that the deceleration timescale coincides with the peak LAT flux time at 0.7 s, the initial bulk Lorentz factor of the short GRB 090510 was calculated to be $\Gamma_0 \sim 2000$ (De Pasquale et al. 2010). Using Γ_0 above the lower limit $\Gamma_{\rm min}$, calculated from $\gamma\gamma$-opacity argument in the simple one-zone model in the prompt phase, Cenko et al. (2011) have modeled the temporally extended X-ray-optical-radio afterglow data of four LAT-detected long GRBs: GRB 090323, GRB 090328, GRB 090902B, and GRB 090926A. A wind environment was preferred for each of these GRBs except for GRB 090902B, for which an ISM environment was preferred (Cenko et al. 2011). Although the sample is rather small, it hints at an interesting trend since a systematic study of well-sampled long GRB afterglows shows that the majority of them is consistent with a uniform density environment (Schulze et al. 2011). The micro-physical parameters, ϵ_e and ϵ_B that we estimated for GRB 110731A in Section 5.3, are lower than for GRB 090510 with $\epsilon_e \sim \epsilon_B \sim 0.1$, which were also estimated from broadband spectral and temporal modeling including LAT data (De Pasquale et al. 2010). Values of ϵ_e and ϵ_B closer to our estimates have been obtained for GRB 090323 with late afterglow data (Cenko et al. 2011).

6. CONCLUSIONS

GRB 110731A is the first long burst detected by instruments on board *Fermi* and *Swift* with simultaneous coverage from optical to gamma rays for a few hundred seconds. Prompt follow-up observations by MOA and late-time data from GROND provide crucial optical data from a few minutes to a few days after the trigger and while the afterglow is still bright in the XRT. The redshift of the burst $z = 2.83$ is relatively high but within the range of other bright long bursts detected by *Fermi*-LAT.

GRB 110731A has a rather high total energy output, with an isotropic-equivalent gamma-ray (10 keV–10 GeV) energy release of $E_{\rm iso} \sim 6 \times 10^{53}$ erg within the prompt phase of the first ∼8.5 s. The brightest peak in the LAT light curve at 5.5 s coincides with peaks in all other energy bands, producing a peak isotropic-equivalent γ-ray (10 keV–10 GeV) luminosity of $\sim 6 \times 10^{53}$ erg s^{-1}. The LAT emission is delayed by ∼2.5 s from the GBM trigger and continues for the next ∼850 s. These features (delayed onset and temporally extended emission in the LAT) are common to many bright LAT bursts. Similarly to other bright LAT bursts, we detect an additional power-law component to the Band function in the time-integrated spectral analysis, with evidence also in the time-resolved analysis, although with lower significance. For GRB 110731A, we also have evidence for a cutoff in the power-law component at GeV energies, although with a significance that is not as high as that measured for GRB 090926A. Indeed, two Comptonized models provide a slightly better fit to the time-integrated spectra from $T_{05,\rm LAT}$ to $T_{95,\rm GBM}$ with respect to the Band plus power-law model. Using a measured variability timescale in the GBM data and by assuming that the LAT photons are cospatial with softer photons, we calculate a jet bulk Lorentz factor of ∼500 from the $\gamma\gamma$ attenuation mechanism producing the GeV spectral cutoff. A value smaller by a factor ∼2 to 3 is also acceptable within modeling uncertainties; for instance, we found ∼300 using a parameterization for two-zone emission models (cf. Section 5.1).

The broadband spectrum of GRB 110731A from optical to $\gtrsim$100 MeV at 550 s, when fitted with a broken power law, together with temporal flux decay behavior in different wavelengths, favors an afterglow wind model as the origin. We interpret the spectral steepening as a cooling break and verify its expected temporal evolution by fitting the broadband spectrum at 2.74 days. The presence of two mild X-ray flares and lack of good optical data at an earlier epoch (III) prohibit us from independently verifying the afterglow model. However, the broadband emission, after extraction of the X-ray flares, is consistent with the model at 550 s. Most remarkably, we find that BAT and LAT spectra at 9 s and 16 s can be fit with single power laws with compatible spectral indices, which in turn are consistent with the measured X-ray spectral index at later times. These broadband spectra at early times strongly suggest their origin as afterglow emission as well. This scenario, however, requires an afterglow onset time before ∼8 s.

With an afterglow onset time of 5.9 s, the first time interval after the brightest LAT peak, we interpret subsequent multi-wavelength data as originating from forward-shock emission in a wind-type medium. We cannot rule out contamination starting at an early time from prompt emission, however. With an initial bulk Lorentz factor ∼500–550 and wind density parameter within the acceptable range we are able to fit and interpret the broadband data. It is worth emphasizing that this second derivation of the bulk Lorentz factor, using the afterglow modeling, is independent from the estimate done using the cutoff

during the prompt phase, but that both numbers are nevertheless very compatible. The resulting micro-physical parameters are $\epsilon_e \sim 3 \times 10^{-3}$ and $\epsilon_B \sim 10^{-2}$, which favor a somewhat larger magnetic energy density than electron energy density in the forward shock. The timescale for the fast-to-slow cooling spectral transition is also compatible with earlier single power-law spectra and later broken power-law spectra. The total isotropic-equivalent jet kinetic energy calculated is $\sim 3 \times 10^{54}$ erg, which puts GRB 110731A among the most energetic bursts.

Compared to other LAT GRBs, GRB 110731A is in the middle of the fluence distribution and is not as bright as the four brightest GRBs, but due to favorable observing conditions we were able to collect comprehensive multiwavelength data and put strong constraints on the temporally extended GeV emission. In addition, both X-ray and optical data strongly suggest the presence of early forward-shock emission in this burst, which would constitute the earliest afterglow emission detected so far among LAT-detected GRBs.

We find that temporally extended LAT emission is compatible with originating from the forward shock that produces the broadband afterglow emission. In the context of this scenario, the delayed onset of the LAT emission can be interpreted as the increasing flux of the forward-shock component, before reaching the deceleration time and after which the traditional afterglow phase begins. The validity of this scenario and the origin of the LAT emission will be further tested by future multiwavelength observations of *Fermi*-LAT-detected bursts.

The *Fermi* GBM collaboration acknowledges support for GBM development, operations, and data analysis from NASA in the US and BMWi/DLR in Germany. The *Fermi*-LAT Collaboration acknowledges generous ongoing support from a number of agencies and institutes that have supported both the development and the operation of the LAT as well as scientific data analysis. These include the National Aeronautics and Space Administration and the Department of Energy in the United States, the Commissariat à l'Energie Atomique and the Centre National de la Recherche Scientifique/Institut National de Physique Nucléaire et de Physique des Particules in France, the Agenzia Spaziale Italiana and the Istituto Nazionale di Fisica Nucleare in Italy, the Ministry of Education, Culture, Sports, Science and Technology (MEXT), High Energy Accelerator Research Organization (KEK) and Japan Aerospace Exploration Agency (JAXA) in Japan, and the K. A. Wallenberg Foundation, the Swedish Research Council and the Swedish National Space Board in Sweden. Additional support for science analysis during the operations phase is gratefully acknowledged from the Istituto Nazionale di Astrofisica in Italy and the Centre National d'Études Spatiales in France.

We gratefully acknowledge the contributions of dozens of members of the Swift team at OAB, PSU, UL, GSFC, ASDC, and MSSL and our subcontractors, who helped make these instruments possible. This work made use of data supplied by the UK Swift Science Data Centre at the University of Leicester. S.R.O. acknowledges support from the UK Space Agency.

Part of the funding for GROND (both hardware and personnel) was generously granted from the Leibniz-Prize to Professor G. Hasinger (DFG grant HA 1850/28-1). T.K. acknowledges support by the European Commission under the Marie Curie Intra-European Fellowship Programme. D.A.K. and S.K. acknowledge support by grant DFG Kl 766/16-1. D.A.K. is grateful for travel funding support through the MPE.

We acknowledge the MOA collaboration to permit target of opportunity observations for GRB afterglow. We also acknowledge the University of Canterbury for allowing MOA to use the B&C telescope. This work was partially supported by the Ministry of Education, Culture, Sports, Science and Technology (MEXT) of Japan.

REFERENCES

Abdo, A. A., Ackermann, M., Ajello, M., et al. 2009a, ApJL, 706, 138
Abdo, A. A., Ackermann, M., Ajello, M., et al. 2011, ApJL, 734, 27
Abdo, A. A., Ackermann, M., Arimoto, M., et al. 2009b, Sci, 323, 1688
Abdo, A. A., Ackermann, M., Asano, K., et al. 2009c, ApJ, 707, 580
Abdo, A. A., Asano, K., Atwood, W. B., et al. 2010, ApJ, 716, 1178
Ackermann, M., Ajello, M., Asano, K., et al. 2011, ApJ, 729, 114
Ackermann, M., Ajello, M., Baldini, L., et al. 2012, ApJ, 754, 121
Amati, L., Frontera, F., & Guidorzi, C. 2009, A&A, 508, 173
Arnaud, K. 1996, in ASP Conf. Ser. 101, Astronomical Data Analysis Software and Systems V, ed. G. Jacoby & J. Barnes (San Francisco, CA: ASP), 17
Arnaud, K., Smith, R., & Siemiginowska, A. 2011, Handbook of X-ray Astronomy (Cambridge: Cambridge Univ. Press)
Asano, K., Guiriec, S., & Mészáros, P. 2009, ApJL, 705, 191
Asano, K., Inoue, S., & Mészáros, P. 2010, ApJL, 725, 121
Atwood, W. B., Abdo, A. A., Ackermann, M., et al. 2009, ApJ, 697, 1071
Band, D., Matteson, J., Ford, L., et al. 1993, ApJ, 413, 281
Baring, M. G., & Harding, A. K. 1997, ApJ, 491, 663
Berger, E., Kulkarni, S. R., Pooley, G., et al. 2003, Natur, 426, 154
Bertin, E., & Arnouts, S. 1996, A&AS, 117, 393
Bhat, P. N., Briggs, M. S., Connaughton, V., et al. 2012, ApJ, 744, 141
Blandford, R. D., & McKee, C. F. 1976, PhFl, 19, 1130
Bošnjak, Ž., Daigne, F., & Dubus, G. 2009, A&A, 498, 677
Breeveld, A. A., Curran, P. A., Hoversten, E. A., et al. 2010, MNRAS, 406, 1687
Breeveld, A. A., Landsman, W., Holland, S. T., et al. 2011, in AIP Conf. Proc. 1358, Gamma Ray Bursts 2010, ed. J. E. McEnery, J. L. Racusin, & N. Gehrels (Melville, NY: AIP), 373
Cardelli, J. A., Clayton, G. C., & Mathis, J. S. 1989, ApJ, 345, 245
Cenko, S. B., Frail, D. A., Harrison, F. A., et al. 2011, ApJ, 732, 29
Chevalier, R. A., & Li, Z.-Y. 2000, ApJ, 536, 195
Corsi, A., Guetta, D., & Piro, L. 2010, ApJ, 720, 1008
De Jager, O. C., Harding, A. K., Michelson, P. F., et al. 1996, ApJ, 457, 253
De Pasquale, M., Schady, P., Kuin, N. P. M., et al. 2010, ApJL, 709, 146
Dermer, C. D. 2004, ApJ, 614, 284
Edelson, R. A., & Krolik, J. H. 1988, ApJ, 333, 646
Evans, P. A., Beardmore, A. P., Page, K. L., et al. 2007, A&A, 469, 379
Evans, P. A., Beardmore, A. P., Page, K. L., et al. 2009, MNRAS, 397, 1177
Fenimore, E. E., Epstein, R. I., & Ho, C. 1993, A&AS, 97, 59
Gehrels, N., Chincarini, G., Giommi, P., et al. 2004, ApJ, 611, 1005
Ghisellini, G., Ghirlanda, G., Nava, L., & Celotti, A. 2010, MNRAS, 403, 926
Giuliani, A., Mereghetti, S., Fornari, F., et al. 2008, A&A, 491, L25
Goldstein, A., Burgess, J. M., Preece, R. D., et al. 2012, ApJS, 199, 19
Granot, J., Cohen-Tanugi, J., & do Couto e Silva, E. 2008, ApJ, 677, 92
Granot, J., & Sari, R. 2002, ApJ, 568, 820
Greiner, J., Bornemann, W., Clemens, C., et al. 2008, PASP, 120, 405
Greiner, J., Clemens, C., Krhler, T., et al. 2009, A&A, 498, 89
Gruber, D., Krühler, T., Foley, S., et al. 2011, A&A, 528, A15
Guilbert, P. W., Fabian, A. C., & Rees, M. J. 1983, MNRAS, 205, 593
Hascoët, R., Daigne, F., Mochkovitch, R., & Vennin, V. 2012, MNRAS, 421, 525
He, H.-N., Wu, X.-F., Toma, K., Wang, X.-Y., & Mészáros, P. 2011, ApJ, 733, 22
Kaneko, Y., Preece, R. D., Briggs, M. S., et al. 2006, ApJS, 166, 298
Kann, D. A., Klose, S., & Zeh, A. 2006, ApJ, 641, 993
Kann, D. A., Klose, S., Zhang, B., et al. 2010, ApJ, 720, 1513
Kann, D. A., Klose, S., Zhang, B., et al. 2011, ApJ, 734, 96
Kouveliotou, C., Meegan, C. A., Fishman, G. J., et al. 1993, ApJL, 413, 101
Krolik, J. H., & Pier, E. A. 1991, ApJ, 373, 277
Krühler, T., Küpcü Yoldaş, A., Greiner, J., et al. 2008, ApJ, 685, 376
Kumar, P., & Barniol Duran, R. 2009, MNRAS, 400, L75
Kumar, P., & Barniol Duran, R. 2010, MNRAS, 409, 226
Kumar, P., & Panaitescu, A. 2000, ApJL, 541, 51
Lithwick, Y., & Sari, R. 2001, ApJ, 555, 540
Lott, B., Escande, L., Larsson, S., & Ballet, J. 2012, A&A, 544, A6
Malesani, D., Leloudas, G., Xu, D., et al. 2011, GCN, 12220, 1
Mattox, J. R., Bertsch, D. L., Chiang, J., et al. 1996, ApJ, 461, 396

McBreen, S., Krühler, T., Rau, A., et al. 2010, A&A, 516, A71
Meegan, C., Lichti, G., Bhat, P. N., et al. 2009, ApJ, 702, 791
Mészáros, P., & Rees, M. J. 1994, MNRAS, 269, L41
Mészáros, P., & Rees, M. J. 1997, ApJ, 476, 232
Nardini, M., Greiner, J., Krühler, T., et al. 2011, A&A, 531, A39
Nicuesa Guelbenzu, A., Klose, S., Krüler, T., et al. 2012, A&A, 538, L7
Norris, J. P., Marani, G. F., & Bonnell, J. T. 2000, ApJ, 534, 248
Nousek, J. A., Kouveliotou, C., Grupe, D., et al. 2006, ApJ, 642, 389
Oates, S. R., Page, M. J., Schady, P., et al. 2009, MNRAS, 395, 490
Oates, S. R., Ukwatta, T., Sakamoto, T., et al. 2011, GCNR, 343, 1
Panaitescu, A., & Kumar, P. 2000, ApJ, 543, 66
Pei, Y. C. 1992, ApJ, 395, 130
Pelassa, V., Preece, R., Piron, F., et al. 2010, arXiv:1002.2617
Piron, F. 2012, in Proc. Conf. Gamma-Ray Burst 2012, PoS(GRB 2012)004, http://pos.sissa.it/archive/conferences/152/004/GRB2012_004.pdf
Poole, T. S., Breeveld, A. A., Page, M. J., et al. 2008, MNRAS, 383, 627
Racusin, J. L., Karpov, S. V., Sokolowski, M., et al. 2008, Natur, 455, 183
Razzaque, S. 2010, ApJL, 724, 109
Razzaque, S., Dermer, C. D., & Finke, J. D. 2010, OAJ, 3, 150
Razzaque, S., Mészáros, P., & Zhang, B. 2004, ApJ, 613, 1072
Rees, M. J., & Mészáros, P. 1994, ApJL, 430, 93
Rossi, A., de Ugarte Postigo, A., Ferrero, P., et al. 2008, A&A, 491, L29
Sakamoto, T., Barthelmy, S. D., Barbier, L., et al. 2008, ApJS, 175, 179
Sari, R. 1997, ApJL, 489, 37
Sari, R., Piran, T., & Narayan, R. 1998, ApJL, 497, 17
Scargle, J. D. 1998, ApJ, 504, 405
Scargle, J. D., Norris, J. P., Jackson, B., & Chiang, J. 2012, arXiv:1207.5578
Schlegel, D. J., Finkbeiner, D. P., & Davis, M. 1998, ApJ, 500, 525
Schulze, S., Klose, S., Björnsson, G., et al. 2011, A&A, 526, A23
Smith, J. A., Tucker, D. L., Kent, S., et al. 2002, AJ, 123, 2121
Tam, P. H. T., Kong, A. K. H., & Fan, Y.-Z. 2012, ApJ, 754, 117
Tanvir, N. R., Wiersema, K., Levan, A. J., et al. 2011, GCN, 12225, 1
Toma, K., Wu, X.-F., & Mészáros, P. 2011, MNRAS, 415, 1663
Tristram, P. J., Fukui, A., Ohnishi, K., Sako, T., & the MOA Collaboration. 2011, GCN, 12242, 1
Ukwatta, T. N., Dhuga, K. S., Stamatikos, M., et al. 2012, MNRAS, 419, 614
Wang, X.-Y., Li, Z., Dai, Z.-G., & Mészáros, P. 2009, ApJL, 698, 98
Yoldaş, A. K., Krühler, T., Greiner, J., et al. 2008, in AIP Conf. Proc. 1000, Gamma-Ray Bursts 2007, ed. M. Galassi, D. Palmer, & E. Fenimore (Melville, NY: AIP), 227
Yonetoku, D., Murakami, T., Nakamura, T., et al. 2004, ApJ, 609, 935
Zhang, B., Fan, Y. Z., Dyks, J., et al. 2006, ApJ, 642, 354
Zhang, B., & Mészáros, P. 2004, IJMPA, 19, 2385
Zou, Y.-C., Fan, Y.-Z., & Piran, T. 2011, ApJL, 726, 2